2D-IR Spectroscopy Determination of CO_2 Solvation Shell Structure and Dynamics in Ionic Liquid-Polymer Composite Material

by

Haoyuan Sun

B.S. in Chemistry, University of Pittsburgh, 2020

Submitted to the Graduate Faculty of

the Dietrich School of Arts and Sciences in partial fulfillment

of the requirements for the degree of

Master of Sciences

University of Pittsburgh

2022

UNIVERSITY OF PITTSBURGH

DIETRICH SCHOOL OF ARTS AND SCIENCES

This thesis was presented

by

Haoyuan Sun

It was defended on

August 18th 2022

and approved by

Sean Garrett-Roe, Associate Professor, Department of Chemistry

Jennifer E. Laaser, Assistant Professor, Department of Chemistry

Rob D. Coalson, Professor, Department of Chemistry

2D-IR Spectroscopy Determination of CO_2 Solvation Shell Structure and Dynamics in Ionic Liquid-Polymer Composite Material

Haoyuan Sun, M.S.

University of Pittsburgh, 2022

Global warming caused as opposed to greenhouse gases, such as carbon dioxide, has become a pressing concern around the world. To help reduce the emission of carbon dioxide, ILs, like ([1-ethyl-3-methylim/idazolium] [bis(trifluoromethylsulfonyl)imide]), have been proposed as point source GHG capture solvents. In this work, the ionic liquid is polymerized with polyethylene glycol diacrylate. Linear spectrum was measured to check the absorbance of the CO_2 in the sample, and 2-Dimensional Infrared (2D-IR) Spectroscopy was used to measure the frequency-frequency correlation function of the system. Preferential solvation is the model that will be established for our system as an alternative to the core-shell-matrix model.

Table of Contents

Preface ix

1.0 Introduction 1

2.0 Background and Theory 9

  2.1 Thermodynamics analysis of CO_2 and N_2 separation and the energy required per mole of CO_2 as a function of the mole fraction of CO_2 9

  2.2 Binding of Amines to CO_2 and the energy cost of this method of CO_2 separation with necessary chemical structures and reaction scheme 12

  2.3 Energy cost of a membrane-based separation and the roles of selectivity and permeability. 13

  2.4 2D-IR theory, and data analysis method 16

  2.5 Fundamental definition of the FFCF, relationship between Ellipticity, CLS, and FFCF, and correlation time, τ_c 19

3.0 Experimental Design and Method 26

4.0 Result and Discussion 28

  4.1 Discrepancy between the result from Kelsheimier and mine 35

5.0 Conclusion 43

6.0 Future direction 44

Bibliography 45

List of Tables

1 Fitting result for 0% sample by *Kelsheimer et al.* 35
2 Fitting result for 10% sample by *Kelsheimer et al.* 36
3 Correlation Time with different center frequency and HWHM 38

List of Figures

1 Structure of the ILs and polymer 4
2 Core-shell-matrix model pictorial depiction 5
3 Concentration of different compositions vs volume percent of ILs in the sample 6
4 Correlation time as a function of the volume percent IL by *Kelsheimer et al* 7
5 The molecular structure of monoethanolamine. 12
6 The temporal setup of the pulse sequence 16
7 The energy level diagram of the interaction after different pulses and the resulting 2D-IR spectrum 17
8 The cartoon of an FFCF 18
9 Frequency trajectory for one molecule as a function of time 19
10 Frequency trajectory as a function of time for another molecule simulated by Langevin Dynamics (a) and the probability density (b) of the ensemble obtained from *Hamm, et al.*[1]. The y axis is labeled as $\delta\omega(t)$, which has the same meaning as $\delta\nu(t)$ 21
11 Two-point frequency correlation function pictorial depiction 24
12 Three vibrational mode for CO_2 26
13 Normalized FTIR spectrum for PEGDA-IL mixture from 0% to 10% (v/v) 28
14 Series of 2D-IR spectra of CO_2 dissolved in IL-PEGDA composite material 29
15 FFCF extracted in spectrum using CLS 31
16 Biexponential fitted FFCF achieved using ellipticity in all samples . . . 32
17 Correlation time for all samples analyzed using the CLS (left) and Ellipticity (on the right). Black bold timescales are the value reported previously[2]. 32
18 FTIR for the 0% ionic liquid sample by Dr. Kelsheimer 37

19 FTIR for the 10% ionic liquid sample by Dr. Kelsheimer 37
20 Biexponential fitted FFCF achieved using ellipticity in all samples . . . 39
21 Correlation time for all samples analyzed using the CLS (left) and Ellipticity (on the right). Black bold timescales are the value reported previously[2]. 40
22 The FFCF extracted using ellipticity for different concentrations. 41
23 The correlation time integrated by each of their FFCF vs IL percentage 41

Preface

I would like to first thank my advisor, Prof. Sean Garrett-Roe, for his guidance and inspiration. It would be difficult for me to learn the fundamental knowledge about 2D-IR and how to think scientifically without such help. Next, I would like to thank my comprehensive exam committee members, Prof. Jennifer Laaser and Prof. Rob Coalson for having faith in me and providing valuable comments and feedback on my research work.

I would like to thank Dr. CJ Kelsheimer, Dr. Sunayana Mitra, Kai Gronborg, Sydney Giles, and Tyler Parrack for helping me understand what 2D-IR is and how to set up 2D-IR measurements. I would also like to thank both undergraduate researchers, Carissa Putruele and Matthew Liberatore, who I am honored to work with over the past year.

I would like to thank my best friend in the department, Dr. Zijian Huo, for all the help academically and mentally. I would also like to thank Victoria Kong, Conner Chee, Benjamin Skultety, Julisa Rozon, Lexi Knight, Tom Staunton, Nick Latiolais, Gilly Ortiz, and all other members from the Laaser lab for the kind and warm welcome.

I would like to thank my parents for supporting me. I started graduate school during the COVID period, and ever since it began, nothing has gone well for me. Teaching, learning, and the way to interact with people have dramatically changed. The past two years have been the toughest time for me in my life, so I would also like to thank myself for not giving up till the end.

Life consists of intertwined choices. Some choices are hard to make because they are right. It is every individual decision that causes the ups and downs in our life, and such decisions make us become who we are. Do not hesitate when making one, and do embrace the result no matter what it is.

1.0 Introduction

Global warming is a serious environmental crisis due to the combustion of fossil fuels to generate power. Carbon dioxide (CO_2) is one of the major components of industry exhaust, and it is also a type of greenhouse gas.

A variety of methods such as absorption, adsorption, and cryogenic distillation[3] have been proposed to capture CO_2 A common amine used in absorption is monoethanolamine (MEA). The main drawback of using MEA as a CO_2 absorbent is its high energy cost for the MEA regeneration process. The carbamate, the product of the MEA reacting with CO_2, is quite stable, and it requires a large amount of heat to separate back to the reactants[4] (detailed calculation in Appendix A). Metal-organic frameworks (MOF) were proposed as an adsorption method[5–8]. Researchers have shown that MOFs are capable of absorbing CO_2 and separating CO_2 from other gases such as H_2[9,10]. Metal-organic frameworks are porous materials, and by combining an amine with a porous material (such as zeolite), the performance of the material will be enhanced[5]. However, MOFs are extremely sensitive to the humidity in flue gas due to their hydrophilicity[7]. A small amount of water could result in the hydrolysis of the bound ligands, and the framework structure would be destroyed[5]. With the flue gas being saturated with water vapor, it takes a large amount of energy to remove the water content before using MOFs to absorb CO_2[5]. Therefore, removing CO_2 using MOFs is not ideal on a large scale. Cryogenic distillation by condensing CO_2 out of the atmosphere has a high energy cost, so large-scale use is impractical[3].

Ionic liquids (ILs) are molten salts at room temperature and consist of only cations and anions. Unlike other salts, which exist in the solid state at room temperature, a bulky side chain is added to each ion to decrease the electrostatic interactions between the ions. Therefore, the melting point decreases[11]. Ionic liquids can absorb CO_2[3,12,13]. Originally, supercritical CO_2 was found to be a good solvent to extract organic compounds, such as naphthalene, dissolved in ionic liquids because it is highly soluble in ionic liquids and could be fully extracted[14]. In later research, ionic liquids' ability to absorb CO_2 was used to separate and capture CO_2 from flue gas[13,15]. Using ionic liquids in industrial CO_2 separation is applicable because of ionic liquids' nonvolatility, stability, and compatibility with other organic solvents and reagents[15]. However, the limiting factor of ionic liquids is their high viscosity, which increases the amount of energy when transferred by pumping[3]. One solution is to encase the ionic liquid with polymer to form a solid membrane[16]. The composite material could take advantage of both the permeability of the polymer and the selectivity of the ionic liquid to make the separation more efficient and easier[12].

Previous research has shown that non-linear spectroscopy of CO_2 could be done in water[17]. Dynamics of CO_2 in ionic liquids were then studied by *Brinzer et al.* using 2D-IR spectroscopy on the anti-symmetric stretching mode[18]. The results showed that the dynamics of CO_2 are dominated by the local diffusive motions, the viscosity, of the cations and anions[18]. Then, the local solvation environments of carbon dioxide in ionic liquids was measured experimentally and modeled computationally[19–22]. The solvatochromic shift of the CO_2 peak in ionic liquids is caused by the solvent cages, and mainly the anions[20,21]. It was also found that the frequency-frequency correlation function is strongly dependent on temperature[22]. After that, the dynamics of CO_2 in ionic liquid-polymer composite systems were measured using 2D-IR spectroscopy[2]. Results show that as the concentration of the polymer increases in the composite material, the solvation shell around CO_2 has a slower reorganization time, which means the solvent exchange will be slower[2]. An unusual "hot ground state" is also found in lower volume percentages of ionic liquid, and it will be discussed later in this document[2].

One of the limitations of ionic liquids is their high viscosity. Instead of pumping the viscous liquid through the line, it is proposed to either polymerize the ionic liquid monomer or polymerize the polymer with the ionic liquid mixed with them to form an IL-polymer mixture. A membrane-based separation has the potential to reduce the energy cost of flowing the ionic liquid. *Bara et al.* showed that polymerized room-temperature ionic liquid could selectively separate CO_2 from N_2 or CH_4, but the permeability could still be improved[23]. *Ueki, et al.* showed that an ionic liquid-polymer composite material has the functionality of an ionic liquid and polymer[12]. *Kelsheimer et al.* showed that a cross-linked IL-polymer composite material has promising CO_2 capturing capability.

Besides polymerizing the ionic liquid with the polymer, individual ions in the ionic liquid could also be polymerized to form a singly-polymerized ionic liquid (SPIL, polymerizing only the cation or the anion) or doubly polymerized ionic liquid (DPIL, polymerize both the cation and the anion). Poly Ionic Liquids (PILs) with a high dielectric constant will have better conductivity and reduced glass transition temperature[24]. The glass transition temperature, T_g, is used to describe the transition of a polymer from a soft, liquid-like state to a hard, glass-like state, and polymers with a low T_g have higher ion conductivity[25]. By doubly polymerizing both the anion and cation, the movement of the ions can be restricted[26]. *Arora, et al.* showed that the mobile contents of a polymeric material can also be changed after polymerization, for example by including the Diels-Alder linkage[27]. PILs are a versatile material.

Due to their properties, such as good mechanical performance, ionic conductivity, thermal stability, and designability, PILs are found to be a good material for flexible strain-humidity bimodal sensors[28]. Polymerized ionic liquids are also used to build Li-ion batteries with good conductivity at room temperature, but one still needs to reduce the interfacial resistance[29–31]. *Liang, et al.* showed that the DPIL can be used to create a lateral p-n junction inside a field effect transistor through the ion locking process, and the polymerized junction could be operated at room temperature[32]. PILs can also capture CO_2[33]. *Karunaweera, et al.* showed that PILs have high permeability and selectivity for a CO_2/N_2 separation, and PILs crossed-linked with 1,3,5-Tris(1'-methylene-3'-vinylimidazolium bistriflimide)benzene (TRI) showed a much longer aging process compared to traditional PILs cross-linked[34]. PILs has the potential to be the next-generation carbon-capture material.

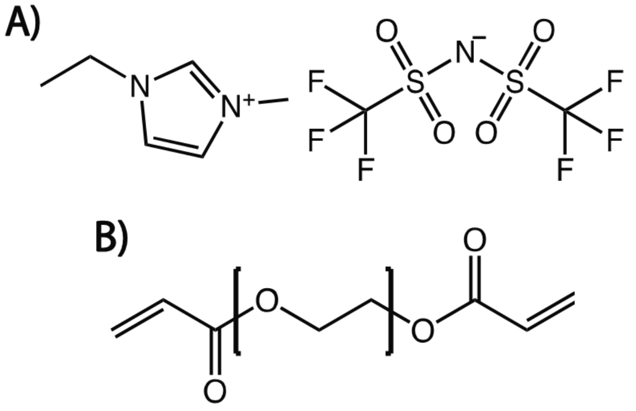

Figure 1: The structure of the ionic liquid, [1-ethyl-3-methylimidazolium] [bis(trifluoromethylsulfonyl)imide] ([emim][Tf_2N]) (a) and the polymer, polyethylene glycol diacrylate (b). The left side of part a is the cation, and the right part is the anion. The photoinitiator used in this experiment is 2,2-Dimethoxy-2-phenylacetophenone (DMPA).

The IL-polymer composite material is selected for this experiment because of its promising CO_2 capture ability[2]. The polymer selected for the composite system was polyethylene glycol diacrylate (PEGDA), and the ionic liquid was [1-ethyl-3-methylimidazolium] [bis(trifluoromethylsulfonyl)imide] ([emim][Tf_2N]). The chemical structure is shown in Figure 1. The physical model of the interaction between the IL and the polymer, the core-shell-matrix model, was proposed by *Kelsheimer et al.* to explain the change of the relaxation time of CO_2 solvation shell in the cross-linked ionic liquid polymer composite system[2].

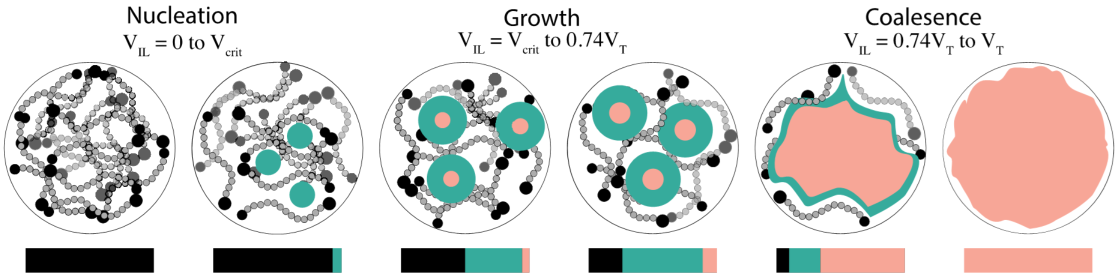

Figure 2: Depiction of the core-shell-matrix model with different ionic liquid-polymer composition[2].

In this model, there are three possible environments for CO_2: bulk ionic liquid (core), the interfacial ionic liquid in the nucleation site (shell), and the bulk polymer (matrix). The proposed depiction for different concentrations of IL is shown in Figure 2. With no ionic liquid present, CO_2 can only interact with the polymer (Figure 2, left). The connected circular chains are representations of the polymer chain. As the ionic liquid is added, until the critical volume, there are more nucleation sites where the IL and polymer interact. The regime between 0% ionic liquid to critical volume of ionic liquid is called the nucleation regime, and the *critical volume* refers to the maximum ionic liquid percentage that would cause the number of nucleation sites to increase rather than increasing the volume of each nucleation site. This is shown as an increase in the presence of the green domain of the Figure, which represents the nucleation site, or the ionic liquid, in the first two diagrams in Figure 2. As the concentration of the ionic liquid keeps increasing after the critical volume before a percent volume of 74%, the size of each nucleation site increases as shown in the middle two figures, where the pink domain inside the green domain represents the bulk-like ionic liquid, and the green circular disk represents the shell-like ionic liquid. The shell-like ionic liquid is the interfacial ionic liquid on the outer surface of the grown nucleation site. This regime is called the growth regime. 74% is the estimated maximum volume taken by the sphere with no overlap in three-dimensional space, which is also known as sphere packing. For the concentration of ionic liquid from 74% to 100% by volume, different nucleation sites start to fuse together because the volume starts to overlap. The physical composition is shown in the fifth diagram in Figure 2 with an irregular shape, and this regime is called the coalescence regime.

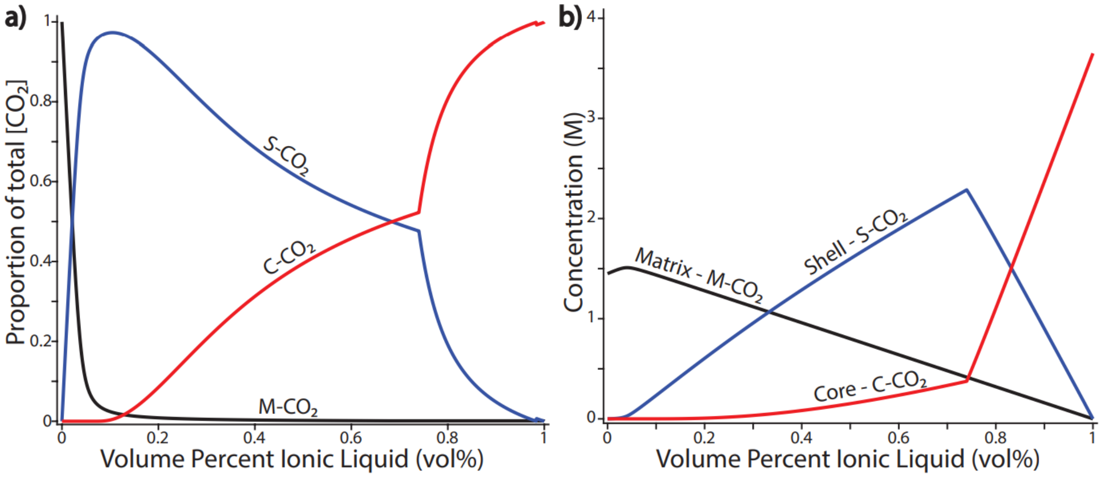

Figure 3: Concentration for different compositions as the volume percent ionic liquid changes (a) and the CO_2 concentration in each component as a function of volume percent of ionic liquid (b).

With the qualitative discussion of the physical composition of the composite material with different IL concentrations, the CO_2 concentration in different environments is shown in Figure 3. Panel a is the ratio of CO_2 in different environments as a function of the IL volume percent, and panel b is the concentration as a function of the IL percent. With no IL present, all CO_2 dissolves in the matrix. In the nucleation regime, most CO_2 is solvated at the shell domain because the number of nucleation sites increases as the IL concentration increases in this regime, and CO_2 is preferentially solvated in the IL. Therefore, the concentration of CO_2 in the shell increases as shown from 0% to the critical volume percent (around 10% by volume of IL). In the growth regime, the concentration of IL increases from the critical volume to 74% as shown in Figure 3b with an increase in both the shell-like and core-like IL. In this region, most CO_2 is solvated in the IL, and the portion of CO_2 solvated in the bulk-like IL increases as CO_2 leaves the interfacial/shell domain. After 74% ionic liquid, the volume of core IL increases drastically since the nucleation sites fuse together, which is shown as a sharp increase in slope after 74% in panel b.

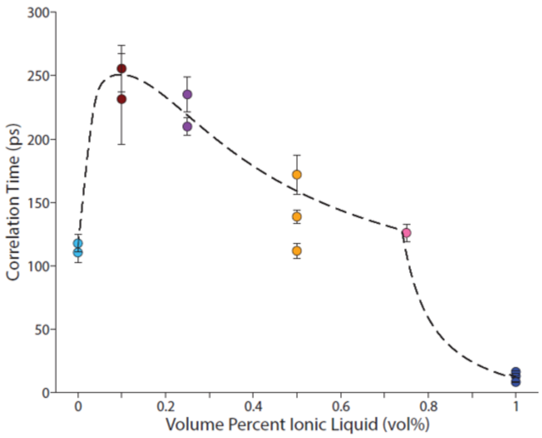

Figure 4: Correlation time as a function of the volume percent IL by *Kelsheimer et al.*[2]. As the concentration of the ionic liquid increases before reaching the critical volume, the time scale increases from 100 ps in the pure polymer. After passing the critical volume, the correlation time keeps decreasing until the IL percentage reaches 74%. After that, the correlation time drops to about 30 ps in the pure ionic liquid.

Results from *Kelsheimer et al.* show the correlation time as a function of ionic liquid concentration (Figure 4)[35]. The correlation time is dominated by the environment of CO_2. The correlation time keeps increasing from the correlation time of bulk polymer (about 100 ps) until the critical volume, and starts to drop down slowly until 74% of the IL volume percentage, and then eventually drops to the correlation time of the pure IL (about 20 ps).

The core-shell-matrix model assumes the spherical approximation for the nucleation site, and this model can be refined since the formation of the nucleation site could be around the polymer backbones. Preferential solvation of CO_2 in the core-shell-matrix model was considered to happen only around the CO_2. However, the preferential solvation between the ionic liquid and the polymer backbone, as well as between the CO_2 and the polymer, has not been taken into consideration. Experimental methods such as atomic force microscopy (AFM), differential scanning calorimetry (DSC), and scanning electron microscopy (SEM) could be used to validate the physical composition of the model. The overall goal of this project is to build an alternative molecular understanding of the intermolecular interactions when the material absorbs the CO_2. The new model will guide the future discovery of promising carbon-capture materials.

2.0 Background and Theory

2.1 Thermodynamics analysis of CO_2 and N_2 separation and the energy required per mole of CO_2 as a function of the mole fraction of CO_2

A detailed derivation is presented by *Socolow, et al.* in an assessment for the APS Panel on Public Affairs[36]. Assume there is a mixture between only CO_2 and N_2 with n moles of gas molecules in total before the treatment, and there is a separation method that could separate only the CO_2 with the efficiency below 100% (not all the CO_2 is absorbed from the gas). The mole fraction of CO_2 is y in the mixture, and the amount of CO_2 would be $y\,n$. The overall amount of CO_2 being captured is denoted as $n_{cap\mathrm{CO_2}}$, the total moles of emitted CO_2 as $n_{emit\mathrm{CO_2}}$, and the total moles of gas emitted as n_{emit}.

The total amount of gas equals the sum of CO_2 captured by the membrane and the emitted gas, which is

$$n = n_{cap\mathrm{CO_2}} + n_{emit}, \tag{1}$$

assuming the only gas being captured by the membrane is CO_2 but not all the CO_2. The captured fraction, α, is the ratio of CO_2 being captured to the overall amount of CO_2 presented in the gas, $y\,n$, which means

$$n_{cap\mathrm{CO_2}} = \alpha\,y\,n, \tag{2}$$

and the amount of CO_2 in the released gas is

$$n_{emit\mathrm{CO_2}} = (1-\alpha)\,y\,n. \tag{3}$$

The amount of gas in the released gas is

$$n_{emit} = n - \alpha\,y\,n = (1-\alpha\,y)\,n. \tag{4}$$

The energy cost of such separation is an entropy-driven process assuming no chemical bond in the separation is formed or broken. The change in entropy is the overall entropy for the emitted gas minus the entropy of the untreated mixture. Entropy is a state function as well, and the change or entropy for gas is calculated using

$$\begin{aligned}\Delta S &= n\,R\ln V_{Final} - n\,R\ln V_{Initial} \\ &= n\,R\ln\frac{V_{Final}}{V_{Initial}}\end{aligned} \tag{5}$$

with V_{Final} being the final volume and $V_{Initial}$ being the initial volume. n is the number of molecules, and R is the gas constant.

The overall amount of CO_2 equals the sum of the amount of CO_2 being captured and released, which is

$$y\,n = n_{cap\mathrm{CO}_2} + z\,n_{emit}, \tag{6}$$

and z is the mole fraction of CO_2 in the emitted gas. To calculate z, the previous expression for $n_{emit\mathrm{CO}_2}$ (equation 3) and n_{emit} (equation 4) were plugged into the previous equation, and the result is:

$$\begin{aligned}z &= \frac{n_{emit\mathrm{CO}_2}}{n_{emit}} \\ z &= \frac{y\,n(1-\alpha)}{(1-\alpha\,y)\,n} \\ z &= \frac{y\,(1-\alpha)}{(1-\alpha\,y)}\end{aligned} \tag{7}$$

The entropy change of each gas in a binary mixture is

$$\begin{aligned}\Delta S_A &= n_A\,R\,\ln\frac{V_A+V_B}{V_A} \\ \Delta S_B &= n_B\,R\,\ln\frac{V_A+V_B}{V_B}\end{aligned} \tag{8}$$

for each gas. V_A is the volume for gas A in the closed system, and V_B is the volume for gas B. The ΔS_{mix}, which is the entropy of the mixture, would be calculated using

$$\Delta S_{mix} = \Delta S_A + \Delta S_B, \tag{9}$$

and by setting the $\frac{V_A+V_B}{V_A}$ and $\frac{V_A+V_B}{V_B}$ being the inverse of mole fraction x^{-1} and $(1-x)^{-1}$,

$$\Delta S_{mix} = -n\,R[x\ln x + (1-x)\ln(1-x)] \tag{10}$$

is the entropy change of separating a binary gas. To calculate ΔS, the change in entropy for the proposed separation,

$$\Delta S = n\,S - n_{emit}\,S_{emit} \tag{11}$$

is the equation, and each unknown in the previous equation is defined as:

$$\begin{gathered} S_{emit} = -n_{emit}\,R\,[z\ln z + (1-z)\ln(1-z)] \\ n_{emit} = n(1-\alpha\,y) \\ S = -n\,R\,[y\ln y + (1-y)\ln(1-y)] \end{gathered} \tag{12}$$

where S_{emit}, the entropy of the emitted gas, and S, the entropy of the untreated mixture, are calculated using equation 10 since both are binary mixture between CO_2 and N_2. The mole fraction for CO_2, z and y, in each environment were used instead of x.

Therefore:

$$\Delta S = n\,R\,\{(1-\alpha\,y)[z\ln z + (1-z)\ln(1-z)] - [y\ln y + (1-y)\ln(1-y)]\} \tag{13}$$

Therefore, the minimum energy for separating two gases per mole of CO_2 is:

$$\begin{aligned} w_{min} &= \frac{T\Delta S}{\alpha\,y\,n} \\ &= \frac{T\,R\,\{(1-\alpha\,y)[z\ln z + (1-z)\ln(1-z)] - [y\ln y + (1-y)\ln(1-y)]\}}{\alpha\,y} \end{aligned} \tag{14}$$

where ΔS is from equation 13, and $\alpha\,y\,n$ is the moles of CO_2 being separated (z could be substituted back into the equation). For instance, a flue gas consists of 15% of CO_2, and the rest of the gas is N_2. The energy consumption per mole of CO_2 from separating 99% of CO_2 from 1 mole of the flue gas at 298 K is

$$\begin{aligned} w_{min} &= \frac{T\Delta S}{\alpha\,y\,n} \\ &= 6869.17\,\text{J per mole of CO}_2 \end{aligned} \tag{15}$$

If the concentration is 400 ppm (0.04%) instead, the same concentration of CO_2 from the atmosphere, the energy cost of CO_2 absorption from 1 mole of the mixture with 99% of the absorption efficiency at 298 K is

$$\begin{aligned} w_{min} &= \frac{T\Delta S}{\alpha\,y\,n} \\ &= 21\,747.78\,\text{J per mole of CO}_2 \end{aligned} \tag{16}$$

2.2 Binding of Amines to CO_2 and the energy cost of this method of CO_2 separation with necessary chemical structures and reaction scheme

To absorb CO_2, one of the existing methods uses amines. One of the amines used is monoethanolamine (MEA), Figure 5.

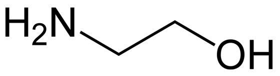

Figure 5: The molecular structure of monoethanolamine.

It was developed to remove acidic gas impurities such as NO_x and SO_x from natural gas streams[4]. According to *Rao et al.*, the main reactions between the MEA and the CO_2 are:

$$\begin{aligned} \textbf{CO}_\mathbf{2}\ \textbf{Absorption:}\ & 2\,R{-}NH_2 + CO_2 \longrightarrow R{-}NH_3{}^+ + R{-}NH{-}COO^- \\ \textbf{MEA Regeneration:}\ & R{-}NH_3{}^+ + R{-}NH{-}COO^- + \text{Heat} \longrightarrow CO_2 + 2\,R{-}NH_2 \end{aligned} \tag{17}$$

with $R = HO{-}CH_2CH_2$. The reaction scheme is the following:

CO_2 Absorption:

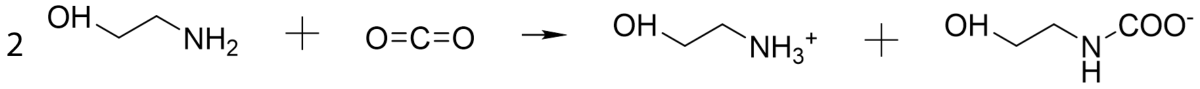

MEA Regeneration:

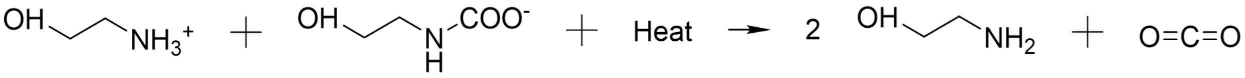

The enthalpy of reaction ΔH of the reaction from a general chemistry perspective could be estimated by measuring the difference between the sum of bond energy for all chemical bonds before the reaction and after the reaction.

The literature value for breaking a N−H bond is 391 kJ/mol. The energy to break a C=O is 745 kJ/mol, but it would be 799 kJ/mol for the one within CO_2. To break a C−N bond, the energy cost is 305 kJ/mol. Lastly, the energy to break C−O is 358 kJ/mol. The enthalpy of reaction (CO_2) absorption could be generally calculated by:

$$\begin{aligned}\Delta H &= 4\text{N}-\text{H} + \text{C}-\text{N} + \text{C}{=}\text{O} + \text{C}-\text{O} - (4\text{N}-\text{H} + 2\text{C}{=}\text{O}) \\ &= \text{C}-\text{N} + \text{C}{=}\text{O} + \text{C}-\text{O} - (2\text{C}{=}\text{O}) \\ &= -305\,\text{kJ/mol} - 745\,\text{kJ/mol} - 358\,\text{kJ/mol} - (-2 \times 799\,\text{kJ/mol}) \\ &= 163\,\text{kJ/mol}.\end{aligned} \tag{18}$$

And the calculation gives an endothermic reaction, which means energy needs to be put in for the reaction to happen. This is counterintuitive because the carbamate bond is stable, and it requires energy to regenerate the MEA. Therefore, literature value was found. Enthalpy of absorption using MEA was measured by *Mathonat et al.*[37]. The enthalpy is -81 kJ/mol at 30% by weight in aqueous solution at 313.15K. This means the absorption process is exothermic. That fits the expectation for energy intake of MEA regeneration. Therefore, the MEA regeneration process will be an endothermic reaction, which means energy needs to be put into the reaction to regenerate the MEA.

2.3 Energy cost of a membrane-based separation and the roles of selectivity and permeability.

An insightful analysis was given by *Mazzotti, M* in his notes for the class Separation Process Technology[38]. Consider the membrane as an ideal semi-permeable membrane placed on a movable piston at the end of the chamber with a mixture of the two gases, and only one type of gas is allowed to pass through the membrane. By moving the membrane across the system, separation is performed because only one species is allowed to pass through the membrane. Gibbs free energy is chosen to calculate the energy of separation since the separating process is assumed to be isothermal and isobaric. The differences are calculated by

$$\Delta G = G_{final} - G_{initial}, \tag{19}$$

and a simplified approach was used for a generic calculation of doing separation using a membrane.

To calculate the energy cost of separation per mole of CO_2 using a membrane, the entropy of sorption in the membrane separation is neglected. Separation using the membrane is an entropy-driven process, and using amine to separate is an enthalpy-driven process. An entropy-driven process has no chemical bond formation or destruction during the reaction. Equation 13 derived in question 2 was used to calculate the entropy for all types of separation of a binary mixture of the gases. Therefore, equation 14 is the energy consumption for membrane-based separation for CO_2.

To calculate the energy consumption per mole for an amine-based separation, Gibbs free energy of the reaction needs to be calculated. The enthalpy of absorption for the MEA-CO_2 absorption process was measured as $-81\,\mathrm{kJ/mol}$ under $313.5\,\mathrm{K}$ in a 30% by weight aqueous solution[37]. According to the equation

$$\Delta G = \Delta H - T\Delta S, \tag{20}$$

the ΔG of the reaction could be calculated as a function of enthalpy, temperature, and entropy. A generic calculation could be performed using the entropy of vaporization for the gas. According to the literature value, the entropy of vaporization of CO_2 is $0.130\,\mathrm{kJ/Kmol}$. By plugging into the equation 20, ΔG of each substance could be calculated as

$$\begin{aligned} \Delta G &= \Delta H - T\Delta S \\ &= -81\,\mathrm{kJ/Kmol} - 298\,\mathrm{K} \cdot (-0.13\,\mathrm{kJ/Kmol}) \\ &= -42.26\,\mathrm{kJ/mol}. \end{aligned} \tag{21}$$

The entropy in the previous calculation was negative because the absorption decreases the overall amount of CO_2, and the entropy of the gas decreases as its volume decreases. The contribution of the entropy to the change in free energy is half the amount of enthalpy. Therefore, the enthalpy of absorption dominates the free energy in an amine-based absorption.

The reaction coefficient could be derived, which determines the fraction of CO_2 reacted with the MEA. To calculate the reaction coefficient,

$$\Delta G = -RT\, \ln K_{eq} \tag{22}$$

and

$$K_{eq} = e^{-\Delta G/RT} \tag{23}$$

were used, and K_{eq} could be used to calculate α, the captured fraction, in equation 2.

By comparing the energy consumption per mole for membrane-based separation and amine-based separation, amine-based separation takes more energy if we assume the same separation efficiency. With the same efficiency, the energy for separation, $T\Delta S$, for both equations would be the same because the final mole fraction of each component is the same, but the amine-based separation needs heat to break the bond in carbamate, and that would make the enthalpy of the reaction larger, which makes the overall energy larger.

The thermodynamics defined previously dictates the energy of reaction and equilibria, while kinetics are defined by selectivity and permeability. The selectivity is defined as[39]

$$\alpha = \frac{P_i}{P_d}, \tag{24}$$

where P_i is the permeability of species i and P_d permeability for species d (this α is different from the one in equation 2). The permeability is defined as

$$P = D\,S \tag{25}$$

that P is the permeability of the membrane, D is the diffusivity of the membrane, and S is the solubility of a specific type of gas in the membrane[40,41]. The Robeson limit, derived by *Robeson et al.*, of a membrane is the upper bound limit between its permeability and selectivity based on experimental data[40,41]. Both the selectivity and permeability define the kinetics of the CO_2 absorption, which correspond to the rate of the reaction.

2.4 2D-IR theory, and data analysis method

Two-dimensional infrared (2D-IR) spectroscopy is a third-order ultrafast nonlinear spectroscopy that measures the vibrational dynamics of a chromophore dissolved in some solvent. The chromophore of this experiment is CO_2 and the solvent is the IL-polymer composite material.

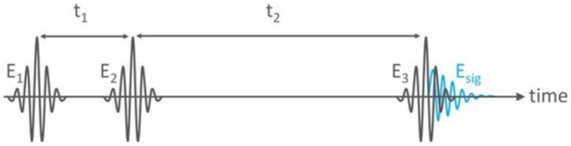

Figure 6: The temporal setup of the pulse sequence, which has three pulses: the first pump (E_1), the second pump (E_2), and the probe pulse (E_3). The first two pump pulses excite the molecule, and the probe pulse detects the final frequency of the molecule. The x-axis of the spectrum, ω_1, is generated by the Fourier Transform of the signal generated in t_1, and the y-axis, ω_3, is generated by separating the frequency using gratings. The signal field is carried with the probe pulse which is called a heterodyne-detected signal, and their intensity is $I = |E_{sig} + E_{LO}|^2$, where E_{sig} is the signal field and the E_{LO} is the intensity of the local oscillator. The detected signal is the real part of the cross-term. The local oscillator is the probe laser that carries the emitted signal field.

At room temperature, most molecules are present in the ground state, and the group of molecules is called an *ensemble*. The experimental setup consists of three pulses: two pump pulses and one probe pulse. The first two pump pulses excite the ensemble to the first excited state, and a waiting time between the second pump pulse and the probe, t_2, is introduced. The probe pulse detects the final frequency of the molecule. As the waiting time increases, spectral diffusion occurs to make the spectrum less stretched along the diagonal and more rounded.

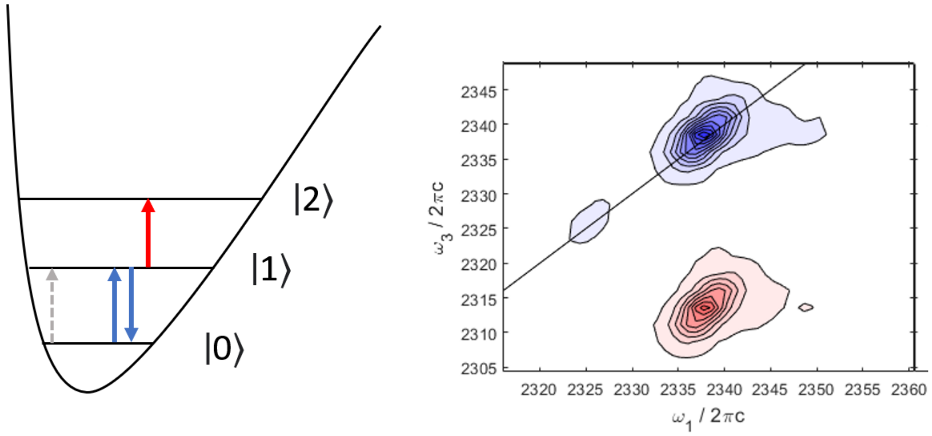

Figure 7: The energy level diagram of the interaction after different pulses (left) and the resulting 2D-IR spectrum (right). There are two pump pulses and one probe pulse interacting with the molecule, and the two pump pulses are simplified in the diagram as the gray arrow. The blue arrows represents the transition between $|0\rangle$ and $|1\rangle$, and the red arrow represents $|1\rangle$ to $|2\rangle$ transition. The color of the arrows matches the color of the peak in the spectrum.

Two pump pulses are simplified as the gray arrow shown in the energy level diagram in Figure 7, and two pump pulses excite some of the molecules to the first excited state. The possible energy transitions for the ensemble with the probe pulse are shown using the colored arrows on the right panel of Figure 7. The three possible interactions lead to the ground state bleach (GSB), stimulated emission (SE), and excited state absorption (ESA). GSB and SE are the interactions between the $|0\rangle$ state and the $|1\rangle$ state. The process of a molecule excited from the $|0\rangle$ state to the $|1\rangle$ state is called GSB, and the process of a molecule stimulated from the $|1\rangle$ state to the $|0\rangle$ state is called SE. ESA is the transition from the $|1\rangle$ state to the $|2\rangle$ state. There are two major peaks with its ω_1 frequency centered at 2337 cm^{-1} in the figure: a blue peak and a red peak. The blue peak represents the transition between the ground state and the first excited states, resulting from the GSB and the SE; the red peak represents the transition between the first excited state and the second state, resulting from ESA.

After the probe pulse interacts with the ensemble, the signal field is dispersed onto an

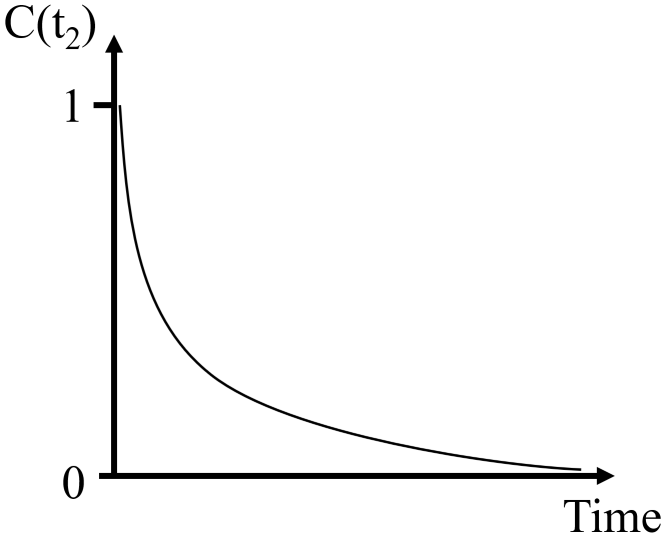

Figure 8: The cartoon of an FFCF is shown here. Its value starts from 1 and decays to 0 as t_2 increases to infinity. This curve is fitted using exponential lines to data extracted from the 2D spectrum plot using CLS or Ellipticity.

MCT by a grating to yield the ω_3 axis.

From the 2D spectrum, the frequency-frequency correlation function, FFCF, is extracted under the *inhomogeneous limit* by measuring the center line slope (CLS) or ellipticity, and all concepts will be discussed in detail later (Section 2.5). The correlation time is fitted using an exponential function after being extracted from each 2D spectrum. A multi-exponential fit, which is used in the data analysis, has the form

$$c(t_2) = \sum_i \Delta_i^2 e^{-t/\tau_i} \tag{26}$$

where Δ_i^2 is the overall frequency value for all samples and τ_i is the timescale for solvent reorganization. The correlation time, or overall timescale, is calculated by

$$\tau_c = \int_0^\infty a_1 e^{-t_2/\tau} dt_2, \tag{27}$$

and the equation will be explained in detail later.

2.5 Fundamental definition of the FFCF, relationship between Ellipticity, CLS, and FFCF, and correlation time, τ_c

The frequency fluctuation correlation function, or the Frequency Frequency Correlation Function (FFCF), is the ensemble-averaged correlation between a frequency at time t and t_0. In order to understand the FFCF, it is necessary to explain the correlation in general. The correlation function is calculated using the time-independent mean frequency, $\bar{\tilde{\nu}}$, and the expected frequency after t_2, which is the waiting time between the second pump pulse and the probe pulse. The difference between the time-independent mean frequency and the instantaneous frequency is

$$\delta\tilde{\nu}(t) = \tilde{\nu}(t) - \bar{\tilde{\nu}}. \tag{28}$$

The FFCF is

$$C(t) = \langle \delta\tilde{\nu}(t)\, \delta\tilde{\nu}(0) \rangle, \tag{29}$$

which is the ensemble average of the product between the frequency fluctuation at time 0 and at time t.

To explain the correlation function, let us start with the antisymmetrical stretch of one CO_2 molecule in PEGDA-[emim][TF_2N] gel, which literature value is 2340 cm^{-1}. The frequency of the molecule fluctuates in time around the center frequency, and it is plotted as a function of time (Figure 9). This figure shows the *frequency trajectory.*

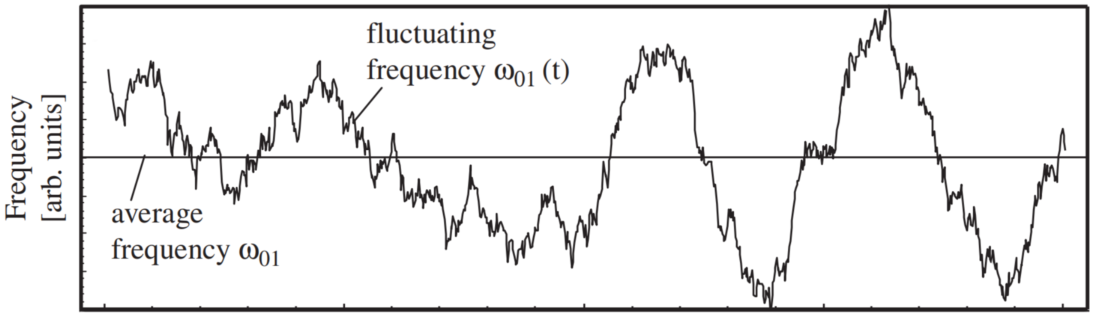

Figure 9: Frequency trajectory for one molecule as a function of time plotted by *Hamm, et al.*[1]. The frequency trajectory of this molecule fluctuates around the average frequency, ω_{01} indicated by the solid straight line in the center.

The starting frequency at time 0, $\tilde{\nu}(0)$ of this molecule, is assumed to be 2345 cm^{-1}, and the difference between that frequency to the mean frequency (the literature value) calculated using equation 28, $\delta\tilde{\nu}(0)$, is 5 cm^{-1}. For a system with n molecules, the ensemble average of the frequency at time 0, $\langle\delta\tilde{\nu}(0)\rangle$, is

$$\langle\delta\tilde{\nu}(0)\rangle = \sum_{i=1}^{n} \frac{\delta\tilde{\nu}_i(0)}{n}, \tag{30}$$

and the correlation function at time 0 is

$$\begin{aligned} C(0) &= \langle\delta\tilde{\nu}(0)^2\rangle \\ &= \sum_{i=1}^{n} \frac{\delta\tilde{\nu}_i(0)^2}{n}. \end{aligned} \tag{31}$$

At time t_2, $\tilde{\nu}(t_2)$, the frequency of the that molecule decreased to 2342 cm^{-1}, and the $\delta\tilde{\nu}(t_2)$ calculated using equation 28 is 2 cm^{-1}. Again, with n molecules in the system, the ensemble average of the frequency at time t_2, $\langle\delta\tilde{\nu}(t_2)\rangle$, is

$$\langle\delta\tilde{\nu}(t_2)\rangle = \sum_{i=1}^{n} \frac{\delta\tilde{\nu}_i(t_2)}{n}, \tag{32}$$

which equals equation 30 because the process is stationary. The correlation function at time t_2 is calculated as

$$\begin{aligned} C(t_2) &= \langle\delta\tilde{\nu}(t_2)\,\delta\tilde{\nu}(0)\rangle \\ &= \sum_{i=1}^{n} \frac{\delta\tilde{\nu}_i(t_2)\,\delta\tilde{\nu}_i(0)}{n}. \end{aligned} \tag{33}$$

Another way to calculate the ensemble average is by grouping molecules with the same frequency together and incorporating the probability density of the frequency distribution into the equation. The frequency trajectory of one molecule is plotted in Figure 10a, and the frequency distribution of a single molecule is plotted as a function, $P(\tilde{\nu}_i)$ in Figure 10b.

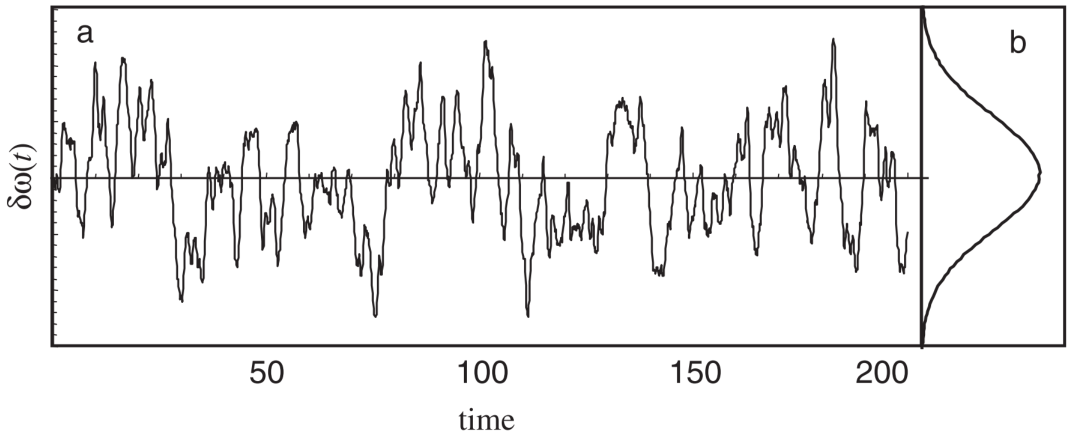

Figure 10: Frequency trajectory as a function of time for another molecule simulated by Langevin Dynamics (a) and the probability density (b) of the ensemble obtained from *Hamm, et al.*[1]. The y axis is labeled as $\delta\omega(t)$, which has the same meaning as $\delta\nu(t)$

With the probability density incorporated, the expression of the ensemble average frequency at t_0, $\langle\tilde{\nu}(0)\rangle$, is rewritten as

$$\langle\tilde{\nu}(0)\rangle = \sum_{i=1}^{n_\nu} \tilde{\nu}_i(0)\, P(\tilde{\nu}_i) \tag{34}$$

with $P(\tilde{\nu}_i)$ being the normalized time-independent probability density of each frequency and n_ν being number of different frequencies. The ensemble average of the difference between the frequency for each molecule and the expected frequency, $\langle\delta\tilde{\nu}\rangle$, is calculated as

$$\begin{aligned}\langle\delta\tilde{\nu}\rangle &= \sum_{i=1}^{n} \delta\tilde{\nu}_i\, P(\delta\tilde{\nu}_i)\\ &= \int_{-\infty}^{\infty} d(\delta\tilde{\nu}_i)\delta\tilde{\nu}_i\, P(\delta\tilde{\nu}_i)\\ &= 0\end{aligned} \tag{35}$$

where the result should be 0 since there should be no difference between the average frequency of the ensemble and the expected frequency. Based on the previous two equations, one-point FFCF at t_0 is

$$\begin{aligned}C(0) &= \langle\delta\tilde{\nu}^2\rangle\\ &= \sum_{i=1}^{n_\nu} \delta\tilde{\nu}_i(0)^2\, P(\tilde{\nu}_i),\end{aligned} \tag{36}$$

and the two-point FFCF at time t_2 is

$$\begin{aligned} C(t_2) &= \langle \delta\tilde{\nu}(0)\delta\tilde{\nu}(t_2)\rangle \\ &= \sum_{i=1}^{n_\nu} \delta\tilde{\nu}_i(0)\delta\tilde{\nu}_i(t_2)\, P(\tilde{\nu}_i, t=0|\tilde{\nu}_i, t=t_2) \\ &= \iint d(\delta\tilde{\nu}_1)d(\delta\tilde{\nu}_3)\, \delta\tilde{\nu}_3\delta\tilde{\nu}_1 P(\delta\tilde{\nu}_1, t=0|\delta\tilde{\nu}_3, t=t_2). \end{aligned} \tag{37}$$

The $P(\tilde{\nu}_i, t=0|\tilde{\nu}_i, t=t_2)$ is the joint probability between the frequency at t_0 and t_2. It is the conditional probability of finding the molecule at frequency $\tilde{\nu}_3$ at t_2 given the molecule with frequency $\tilde{\nu}_1$ at ${t_0}^1$. The probability distribution of t_0 and t_2 are the same because the frequency fluctuation is static. As shown in equation 35, we can prove that the $\delta\tilde{\nu}_i$ is an odd function centered at the expected frequency using equation 28, and the probability density should be a Gaussian function centered at the expected frequency, which means an even function, based on the Central Limit Theorem. Therefore, the product is an odd function, and the integration of an odd function over all values is 0. The value of the correlation time would reach its maximum because there it is the square of the initial value. As time increases, more frequency fluctuates around the center frequency, (*e.g.* passing from over the expected frequency to below the expected frequency), and that results in a negative value of the product in the FFCF. The negative value decreases the integration of the FFCF, and eventually, the FFCF reaches 0 after the time passes far beyond the correlation time, τ_c.

Correlation time is the time that takes the initial frequency at t_0 to be non-correlated with the final frequency at t_2. It is calculated from the correlation function. Analytically, the correlation time is also defined as

$$\tau_c = \int_0^\infty \frac{\langle \delta\tilde{\nu}(0)\delta\tilde{\nu}(t_2)\rangle}{\langle(\delta\tilde{\nu})^2\rangle} dt_2. \tag{38}$$

The $\langle \delta\tilde{\nu}(0)\delta\tilde{\nu}(t_2)\rangle$ in the numerator is the FFCF, and the $\langle(\delta\tilde{\nu})^2\rangle$ in the denominator is used as the normalization to make the maximum value of this function to be 1. Graphically, τ_c is the area under the correlation function, which is shown in Figure 8. The meaning of this value is the time that how much the final frequency, ω_3, deviates from the initial frequency, ω_1.

By convention, in most publications in this field, the frequency is expressed in ω, angular frequency, rather than in $\tilde{\nu}$, wavenumber. Therefore, after switching terms and changing $\delta\tilde{\nu}_i$ to ω_i, the conventional expression is

$$C(t) = \iint \omega_1\omega_3\, P(\omega_1, t = 0|\omega_3, t = t_2)\, d\omega_1\, d\omega_3. \tag{39}$$

A typical 2D-IR spectrum has the same shape as the joint probability density, and the plot of the correlation function is proportional to the spectrum. This means ideally if we take a spectrum at t_0, it should have the shape of a straight line. To calculate the correlation time, the response function needs to be extracted from the spectrum. The response function represents the third-order responses of the dipole.

$$\begin{aligned} R_1^{(3)}(\omega_1, t_2, \omega_3) &= \int_0^\infty \int_0^\infty R_1^{(3)}(t_1, t_2, t_3) e^{i(\omega_3 t_3 - \omega_1 t_1)} dt_1 dt_3 \\ R_2^{(3)}(\omega_1, t_2, \omega_3) &= \int_0^\infty \int_0^\infty R_2^{(3)}(t_1, t_2, t_3) e^{i(\omega_3 t_3 + \omega_1 t_1)} dt_1 dt_3 \end{aligned} \tag{40}$$

There are two types of response functions. The first type is rephasing, which is indicated by $R_1^{(3)}$ in equation 40, and the second one is non-rephasing, which is indicated by $R_2^{(3)}$ in equation 40. Using these two equations, the purely absorptive spectrum is calculated using

$$R^{(3)}(\omega_1, t_2, \omega_3) \equiv \mathrm{Re}[(R_1^{(3)}(\omega_1, t_2, \omega_3) + R_2^{(3)}(\omega_1, t_2, \omega_3))].^{1} \tag{41}$$

The real part of the sum of the two response functions is the absorptive spectrum. The absorptive spectrum is equal to the joint probability density within the limit of inhomogeneous broadening. A key assumption, called the *inhomogeneous limit*, is made, which means the frequency fluctuations are not changing during the relevant portions of t_1 and t_3. Within this limit, the joint probability density in the previous equation is proportional to the response function. It is written as

$$C(t_2) \equiv \int_{-\infty}^{\infty} \int_{-\infty}^{\infty} \omega_1\omega_3 R^{(3)}(\omega_1, t_2, \omega_3) d\omega_1\omega_3, \tag{42}$$

which is almost the same as equation 39, but uses the response function to estimate the real probability density.

The spectrum is an estimation of the joint probability density under the inhomogeneous limit. As shown in Figure 11, the initial frequency fluctuation, ω_1, is plotted on the x-axis, and final frequency fluctuation, ω_3, is shown on the y-axis. The colored area is the integration of the FFCF. When t_2 is 0 (in panel a), the integration is at its maximum since it is $\langle \omega_1^2 P(\omega_1) \rangle$, and every value is positive. A short time after the first laser pulse (in panel b), the frequency fluctuation starts to change sign compared to ω_1, and that decreases the FFCF. Lastly (in panel c), the differences in final frequency is completely uncorrelated compared to ω_1, and the shape will be round. The integration is 0.

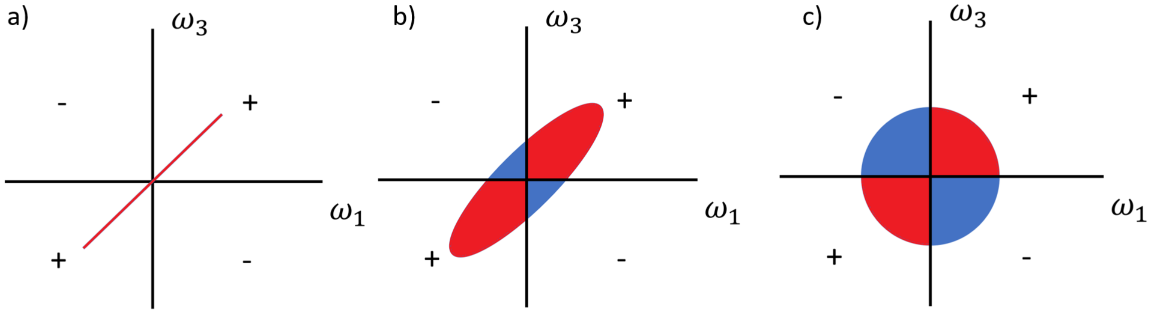

Figure 11: The qualitative figure of the product for the two-point frequency correlation function. Three example times are shown: a) when $t_2 = 0$, b) when $0 < t_2 < \tau_c$, and c) when $t_2 \gg \tau_c$. Red in the figure represents a positive value for the indicated quadrant, and blue represents a negative value for that quadrant.

For example, if the initial frequency for the antisymmetric stretch for a CO_2 molecule is 2342 cm^{-1} with the expected frequency being 2340 cm^{-1}, ω_1 frequency is 2cm^{-1}. After a short time, the frequency becomes 2338 cm^{-1}, and the ω_3 is $-2\,cm^{-1}$. Such changes from a positive difference to a negative difference results in a negative contribution to the integral (equation 42). Finally, after $t_2 \gg \tau_c$, there is an equal probability of the final frequency having the same sign as the initial frequency or different compared to the initial frequency. Therefore, the area of the negative value is the same as the area of the positive value.

In the previous discussion, it has been shown that the spectrum is used to estimate the joint probability density. Therefore, the FFCF can be extracted from the experimental spectrum. The normalized FFCF has its maximum in the initial condition and decays to

0 after a long time. Methods such as Center Line Slope (CLS) or ellipticity are used to calculate the FFCF[42,43]. CLS is the method to extract the slope of the linear fit of the extrema. Slices of each spectrum are taken along the ω_1 axis, and the peak is fitted to a Voigt function, a convolution of a Lorentzian and a Gaussian function. After that, a linear fit is done on the extrema. Then, the slope of the linear fit and the standard deviation are extracted from the half-width-half-max. The FFCF extracted by CLS decays from the maximum value (< 1) at $t_2 = 0$ to zero at t_2 when t_2 approaches infinity. For short t_2, the spectrum is strongly correlated, and the value of the slope is high. For longer t_2, the spectrum will be less correlated, which means the slope will be 0 ideally. This is one way to measure the joint probability density. Ellipticity is another way that uses a 2-dimensional Gaussian function to extract the correlation information. It is calculated by fitting the intensity profile of the peak to

$$I = \exp\left\{\frac{-(\omega_1 + \omega_3)^2}{2\sigma_a^2}\right\} \exp\left\{\frac{-(\omega_1 - \omega_3)^2}{2\sigma_b^2}\right\} \tag{43}$$

where the first term with $\omega_1 + \omega_3$ is the term describing the shape of the peak along the diagonal and the second term with $\omega_1 - \omega_3$ describing the shape along the anti-diagonal. σ_a determines the diagonal width of the spectrum, and σ_b determines the anti-diagonal width. The FFCF is calculated using the equation

$$C = \frac{\sigma_a^2 - \sigma_b^2}{\sigma_a^2 + \sigma_b^2}. \tag{44}$$

In general, for a small t_2, the anti-diagonal width is extremely small compare to longer t_2. Therefore, the correlation value is close to 1. As t_2 increases, so will σ_a and the resulting ellipticity will approach zero. If the spectrum represents the true joint probability density of the function, both CLS and ellipticity would give the exact result of the FFCF and correlation time, i.e. a function decaying from 1 to 0. The spectrum is not an ideal elliptical shape, and the ellipticity works the best when the spectrum is elliptical.

3.0 Experimental Design and Method

1-ethyl-3-methylimidazolium bis(trifluoromethylsulfonyl)imide ([emim][TF2N]) (Iolitec) and poly(ethylene glycol) diacrylate (PEGDA, from Sigma-Aldrich, M_n=700, CAS# 26570-48-9, Lot# MKCC7963) were vacuum dried. For each sample, the designated amount of ionic liquid and polymer was transferred into a vial and mixed overnight. Each sample was then prepared by transferring 1 μL of the mixture into two calcium fluoride windows with a 12 μm Teflon spacer. Samples were then cross-linked under a 36 W UV lamp (MelodySusie). Tubes were connected to the sample cell and the pressurized bone-dry CO_2 (Matheson) was pumped into the sample through the inlet valve. The only space for the CO_2 to flow through the apparatus was between the two CaF_2 windows. As the CO_2 passed through, it was absorbed by the IL gel. After that, Fourier-transform infrared spectroscopy (FTIR) spectra were taken for each sample using a Nicolet 6700 FTIR spectrometer.

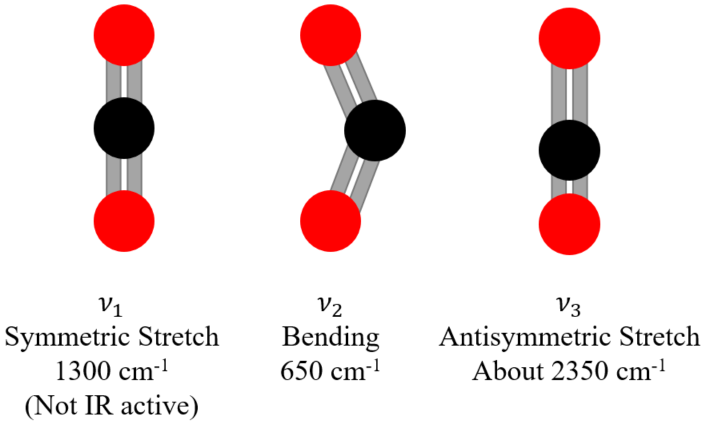

Figure 12: Three vibrational mode for CO_2. In gas phase, ν_1, the symmetrical stretch, is about 1300 cm^{-1}, and ν_2, the bending motion, is about 650 cm^{-1}, and the ν_3, the anti-symmetrical stretch, is about 2350 cm^{-1}. All transitions are from the ground state to the first excited state.

Transmission FTIR spectroscopy is linear spectroscopy, which means there is one electric field interaction. CO_2 has three vibrational modes, which are a doubly degenerate bending motion (about 650 cm^{-1} in the gas phase), a symmetric stretch (about 1300 cm^{-1} in the gas phase), and an anti-symmetric stretch (about 2350 cm^{-1} in the gas phase). In the condensed phase, the main peak resulting from the anti-symmetrical stretch is around 2336 cm^{-1} and a shoulder band which is about 20 cm^{-1} less than the main peak, which is a result of molecules with thermally excited bending motion. This is called the "hot band," (Figure 9). To measure the dynamics of the CO_2, 2D-IR measurements were carried out to measure the FFCF of the sample.

The Coherent Vitesse oscillator pumped by the Coherent Verdi Nd:YVO_4 laser was used to generate the mode-locked pulses. Then, the Coherent Legend Elite chirped pulse amplifier is used to amplify the output seed laser from the oscillator to generate 4 W, 5 kHz rate, and 803 nm laser pulse. The optical parametric amplifier (OPA) is built to generate the mid-infrared femtosecond laser pulse[44] with 1 W of the 803 nm laser input from the OPA. The 2D spectrometer is set after the OPA to generate the correct pulse sequences[45]. In the 2D spectrometer, the incoming laser is split into pump pulses and probe pulses. Two pump pulses are separated temporally using a Mach-Zehnder interferometer. The probe pulse is spatially separated into the real probe and the reference, and it is separated with the second pump pulse using a delay stage. A HeNe laser with a wavelength of 632.8 nm is used as the internal clock of the spectrometer, and the signal is generated by doing a Fourier transformation to the time-domain signal collected using Mercury-Cadium-Telluride (MCT) detector chilled with liquid nitrogen.

4.0 Result and Discussion

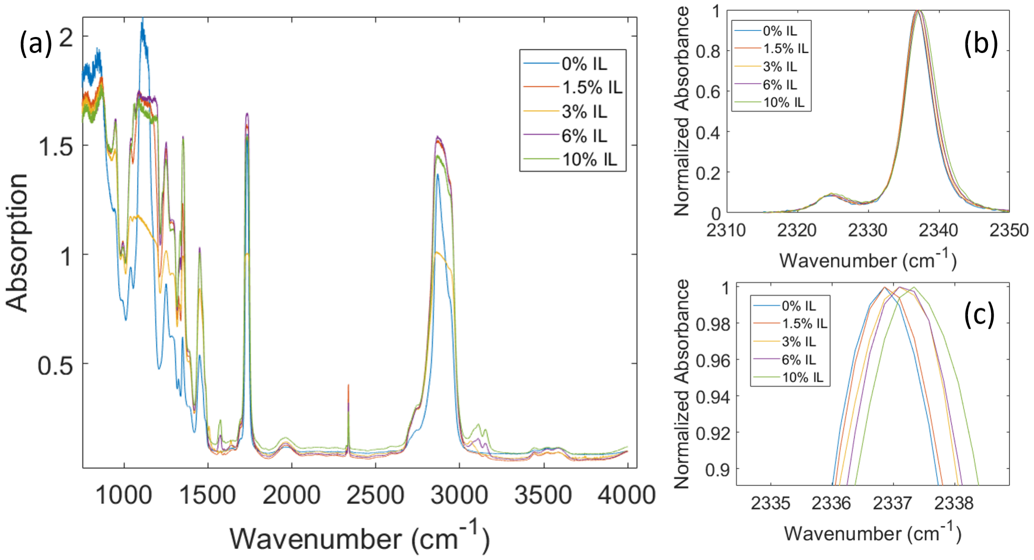

Figure 13: Normalized FTIR spectrum for PEGDA-IL mixture from 0% to 10% (v/v). As the concentration of ionic liquid increases, the peak red-shifts. The peak at ~2325 cm^{-1} is due to the thermally excited bending motion of some CO_2 molecules at room temperature, called the "hot band."

FTIR spectra were taken for each sample after flowing CO_2 into the sample cell (Figure 13). The distinct peak at 1700 cm^{-1} indicates that the sample is crosslinked (Figure 13a). The anti-symmetrical vibrational peak was found at around 2336 cm^{-1}. As the volume percent of the ionic liquid increases, the peak red-shifts. This result is consistent with the reported frequency of the center peak[2]. Each sample also has a shoulder peak at 2325 cm^{-1}. The transition energy for the bending motion is 667 cm^{-1} in the IL[18], therefore the difference between the ground state and the first excited state for the bending motion is 650 cm^{-1}. The ratio between molecules at the first excited, doubly-degenerated bending motion, E_b, and the ground state, E_a, can be calculated by plugging values into the Boltzmann equation

$$\begin{aligned}\frac{N_b}{N_a} &= \frac{g_b}{g_a}\exp\left(\frac{-(E_b - E_a)}{k_B T}\right) \\ &= \frac{2}{1}\exp\left(\frac{-667\text{cm}^{-1}}{207\text{cm}^{-1}}\right) \\ &= 0.080 = 8.0\%\end{aligned} \tag{45}$$

where $k_B T$ is roughly 207 cm^{-1} at room temperature and the bending motion is the same in the condensed phase. Therefore, the intensity of the hot band is about $\frac{0.080}{1+0.080}$, which is about 7.4% of all the CO_2 at room temperature.

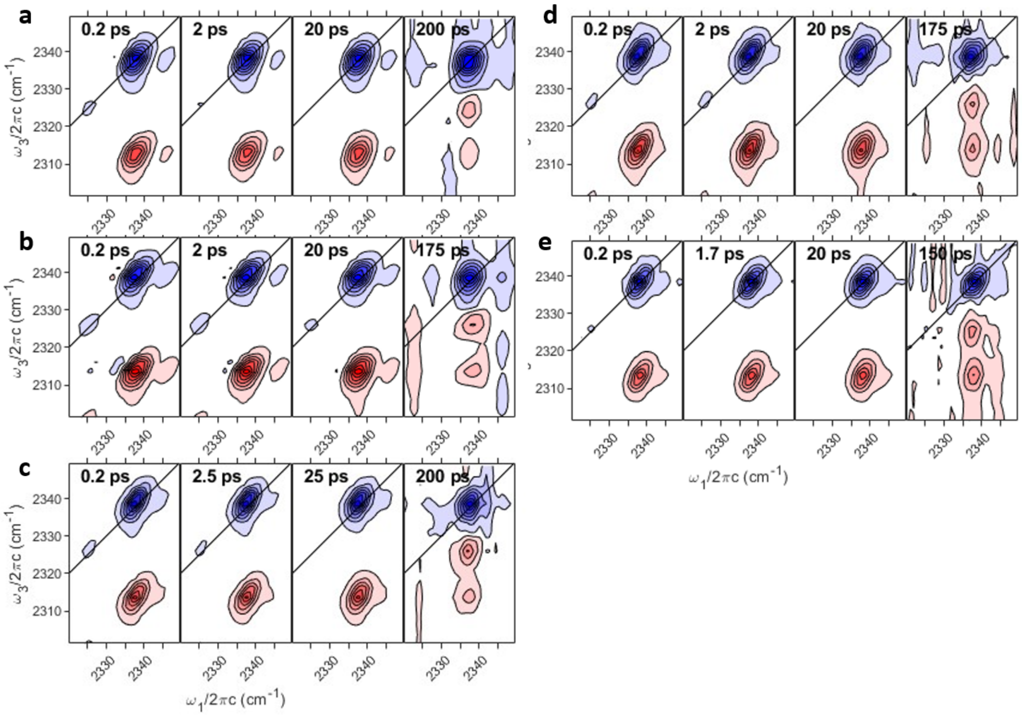

Figure 14: Series of 2D-IR spectra of CO_2 dissolved in IL-PEGDA composite material. Panel a) is 0% IL, which is pure PEGDA; panel b) is 1.5% IL; panel c) is 3% IL; panel d) is 6% IL; panel d) is 10% IL. At an early time point such as 0.2 ps, the spectrum is strongly correlated, and the peak is stretched along the diagonal. Due to spectral diffusion, the peak gets rounded and less correlated along the diagonal. The hot ground state starts to appear at longer waiting times, which is the red peak between the blue peak, generated by GSB and SE, and the red peak, generated by ESA.

2D-IR spectra are shown in Figure 14. In a 2D-IR spectrum, the x-axis is the initial frequency, ω_1, and the y-axis is the final frequency, ω_3. The waiting time, t_2, is the time delay shown in Figure 6. As t_2 increases, the spectrum will inhomogeneously broaden along the diagonal direction and homogeneously broaden along the anti-diagonal direction. For example, in Figure 14a, the spectrum evolves in time from being correlated at 200 fs (i.e., the spectrum is elliptical along the diagonal) to non-correlated at 200 ps (i.e., the spectrum is rounded).

To better explain the spectrum, bra-ket notation is used to indicate changes in the energy level. According to the symmetry of the vibrational mode, three quantum numbers are used in sequence to represent the state of the CO_2 molecule, $|\nu_1\nu_2^l\nu_3\rangle$. ν_1 represents the symmetrical stretch, ν_2 represents the bending motion, ν_3 represents the anti-symmetric stretch, and l represents the vibrational angular momentum quantum number. The symmetrical stretch is not IR active, which means it cannot be detected using IR spectroscopy. Therefore, only two quantum numbers are used, because the first quantum number that represents the symmetrical stretch is omitted. The main blue peak in the spectrum can be written as the transition energy between $|0^00\rangle$ and $|0^01\rangle$, and the main red peak could be written as the difference in energy between $|0^01\rangle$ and $|0^02\rangle$. The blue peak located in 2325 cm^{-1} on each axis with less intensity is the "hot band" discussed in the linear spectrum. The "hot band" is generated by the ensemble of CO_2 molecules with excited bending motion, $|1^10\rangle$, at room temperature when the two pump and probe pulses interact with the molecule. A new peak appears between the major blue peak and red peak, at $(\omega_1, \omega_3) = (2340\mathrm{cm}^{-1}, 2325\mathrm{cm}^{-1})$, and is called the "hot ground state". The "hot ground state" is generated when the pump pulse interacts with the molecule, the molecule is excited to the first excited state, which is $|0^01\rangle$, and then thermally relaxes down to the "hot ground state", $|1^10\rangle$, during t_2. It is generated by thermal relaxation because the transition from $|0^01\rangle$ to $|1^10\rangle$ is not permitted based on the selection rules. Thermal relaxation is caused by the system-bath coupling. On the molecular level, it is caused by the inelastic collision between the molecule and its surroundings.

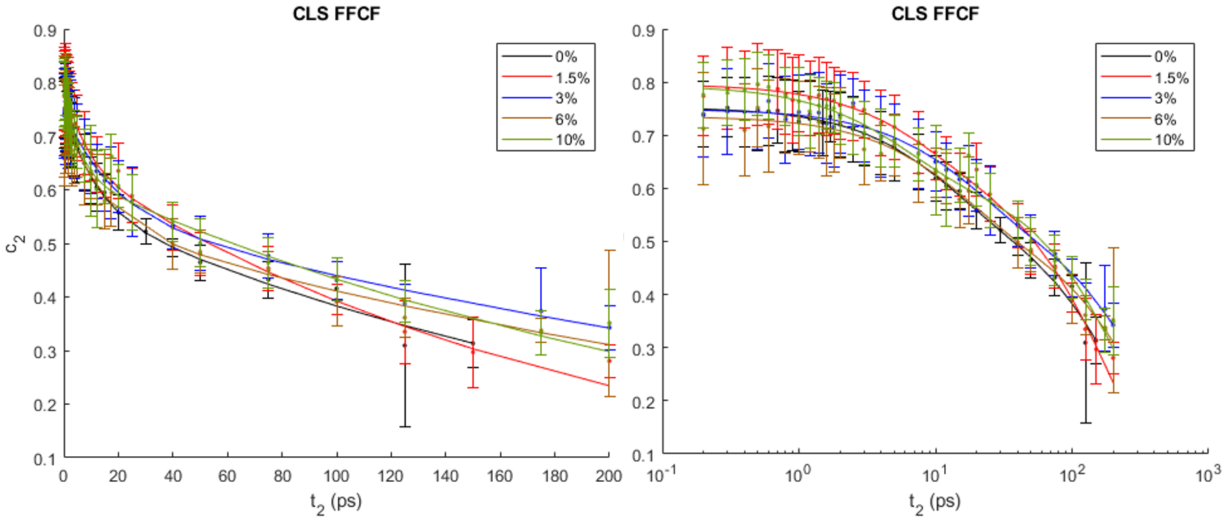

Figure 15: The FFCF extracted in each spectrum using CLS has been plotted based on the normal time axis (left) and log-based time axis (right), and the data points are fitted to the sum of three exponential function denoted as c_2. The curve decreases drastically at short t_2, and it decreases slowly for longer t_2.

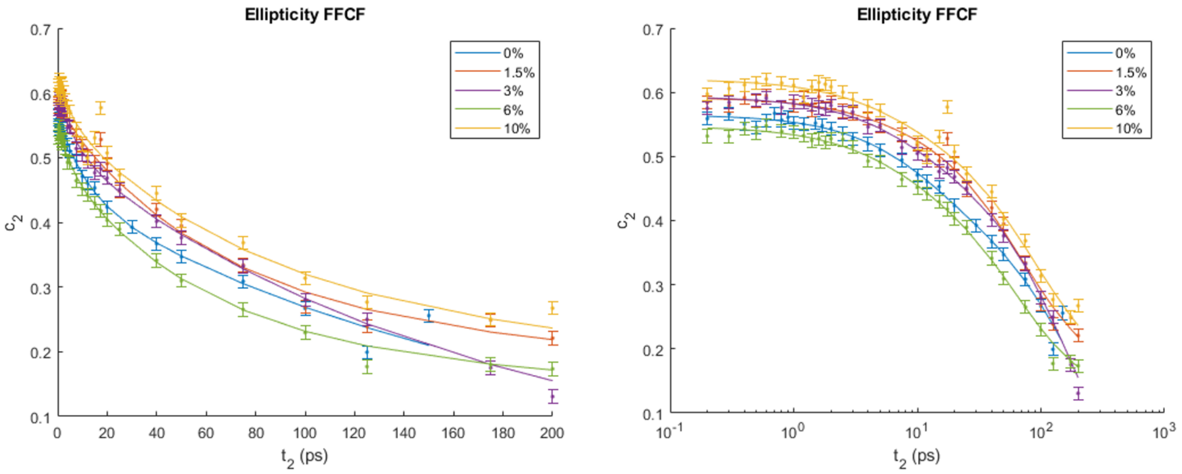

Figure 16: Biexponential fitted FFCF achieved using ellipticity in all samples. The left is the regular time-based axis, and the right is the log-based time axis. During the fitting, some of the error bars were turned off since the error was too high. The error bar in this figure is not a good indication of the realistic size of the uncertainty.

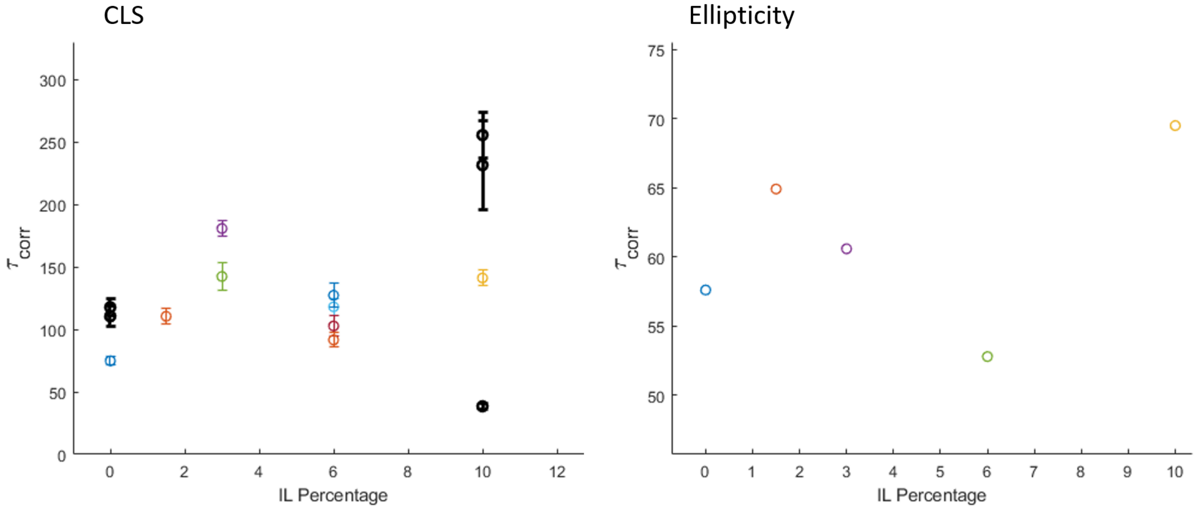

Figure 17: Correlation time for all samples analyzed using the CLS (left) and Ellipticity (on the right). Black bold timescales are the value reported previously[2].

The frequency-frequency correlation function (FFCF) can be extracted from the spectrum, and that function gives the correlation time of the system. One of the methods is center line slope (CLS), which is analyzed deeper in Appendix B. Figure 15 shows the FFCF extracted using CLS, and the integration of each correlation function is shown in the left panel (Figure 17) together with the reported value by *Kelsheimer et al.* The data in this word does not agree with the result from *Kelsheimer et al.*, because the error bar does not overlap. In Figure 15, the black curve, the 0% IL sample, has the lowest area under the curve, and it corresponds to the lowest correlation time in Figure 17. The blue curve, which is the 3% IL, in Figure 15 has the largest area under the curve visually, and it corresponds to the highest correlation time for the 3% sample in Figure 17.

Ellipticity is used due to some systematic error in the fitting using CLS, and it is also analyzed deeper in Appendix B. Data shown in Figure 16 is integrated correctly based on the right panel in Figure 17. The green curve, which represents the 6% IL data, has the lowest area under the curve, and that matches the lowest correlation time in Figure 17; the yellow curve in Figure16, which is the 10% data, has the largest area under the curve, and it matches the highest correlation time in Figure 17. The correlation time increased from 0% to 1.5% and then decreased from 1.5% to 6% and then rose again to a higher point at 10%. This trend is unexpected because *Kelsheimer et al.* showed an increase from 0% to 10%. The correlation time extracted using the ellipticity is also strongly dominated by the last data point, which is the 200 ps correlation time. In the left panel of Figure 16, the 3% data has a steeper regression because the time point at 200 ps is lower compared to other sets. In the same figure, the 10% data has more steady decay because the last data point is higher than the rest. On the scale from 0 ps to 200 ps, it does not affect the correlation time much as shown in Figure 17. However, the correlation time will be affected if the integration is longer.

It is hard to compare the FFCF extracted from CLS and ellipticity. The FFCF extracted from CLS used a biexponential, and it was integrated from 0 ps to infinity. The FFCF extracted using ellipticity used a triexponential, and it is integrated from 0 ps to 200 ps. Both integration time and the number of exponential fitting functions are different, which made it difficult to compare the results.

Based on the data, the claim by *Kelsheimer et al* can neither be supported nor rejected. In the future, the 2D-IR measurement will be carried out with a higher signal-to-noise ratio. Mass transfer of the sample will also be recorded more carefully, and the cosolvent will be used to transfer and mix the polymer and ionic liquid to maximize the homogeneity of the sample. As for the data analysis, it is important to re-analyze the data with the same biexponential fit using CLS and ellipticity, and the integration bounds of the fitting will be adjusted to match each other.

As stated in the previous discussion, the goal of this research is to build a molecular understanding of the model to guide future research on finding a better model for carbon capture, and the alternative is the preferential solvation model since the solvent molecule is not distributed around the solute molecule homogeneously[46]. The equation for our system could be derived from the work done by *Dunbar, et al.* They have shown that the solvent mixture composed of DMF and D_2O results in preferential solvation of a metal carbonyl compound, biotin hydrazide benzoyl chromium tricarbonyl. In that solvent system, the correlation time is defined by three components: D_2O, DMF, and the exchange part between the two solvents. Each component has its own weighing factor. Changing the concentration would lead to changes in the weighing factors. Assuming solvent exchange dynamics do not contribute to the spectral diffusion timescale, and D_2O and DMF have a similar time scale, the FFCF timescale could be generalized to

$$C(t) = x_{(DMF)}e^{(-t/\tau_{solvent})} + \frac{1}{\beta}(1 - x_{(DMF)})e^{(-t/\tau_{exch})}, \tag{46}$$

where $C(t)$ is the correlation time of the system, x_{DMF} is the mole fraction of DMF, $\tau_{solvent}$ is the correlation time for the pure solvent since the two species are assumed to have similar correlation times, τ_{exch} is the correlation time for the solvent exchange, and β is the concentration-independent parameter that adjusts spectral diffusion based on exchange dynamics. The assumption that D_2O and DMF have the same time scale does not apply to our model since the time scale for the ionic liquid is 30 ps and 100 ps for the PEGDA. By plugging in their D_2O time scale and DMF time scale as a different term into the previous equation, the equation would be

$$C(t) = w_{\mathrm{IL}}e^{(-t/\tau_{\mathrm{IL}})} + w_{\mathrm{PEGDA}}e^{(-t/\tau_{\mathrm{PEGDA}})} + \frac{1}{\beta}(1 - x_{\mathrm{PEGDA}})e^{(-t/\tau_{shell})}. \tag{47}$$

where w_{IL} is the concentration of ionic liquid, w_{PEGDA} is the concentration of PEGDA, and τ is the correlation time for each composition. Preferential solvation reduces the complexity of the fitting function compared to the core-shell-matrix model.

4.1 Discrepancy between the result from Kelsheimier and mine

Only two samples, 0% and 10% ionic liquid mixtures, are replicants with reported value by *Kelsheimer et al.*. The reported data are analyzed using CLS. The Correlation time reported by Dr. Kelsheimer for the 0% sample prepared in May 2019 is 117.8 ps with the standard deviation being 6.8 ps, and the correlation time for the 10% ionic liquid sample prepared in September 2018 is 255.5 ps with the standard deviation of 18.3 ps. A bi-exponential fit,

$$y(x) = a_1 e^{-x/t_1} + a_2 e^{-x/t_2} \tag{48}$$

is used to fit the spectrum, and the fitting result for the 0% data is shown in table 1, and the 10% fitting result in table 2.

Table 1: Fitting result for 0% sample by *Kelsheimer et al.*

Coefficients	Value	Uncertainty Range
a_1	0.228	(0.2041, 0.2519)
a_2	0.491	(0.4717, 0.5104)
t_1	17	(13.9, 20.3)
t_2	232	(219, 244)

Table 2: Fitting result for 10% sample by *Kelsheimer et al.*

Coefficients	Value	Uncertainty Range
a_1	0.179	(0.159, 0.199)
a_2	0.5263	(0.506, 0.547)
t_1	18.55	(14.2, 22.9)
t_2	479	(413, 544)

The biggest problem with replicating the result comes from pre-set parameters for the fitting. There are a couple of parameters, including half-width-at-half-maximum (HWHM, calculated by finding the width between half of the peak value then dividing by 2), center frequency, anharmonicity, etc. for fitting the spectrum to get the correlation time. With different parameters, the result of the calculated FFCF and correlation time is different. Unfortunately, those parameters were not found in the material from *Kelsheimer et al.*. The center frequency and the HWHM is found in the linear spectroscopy, which is shown in Figure 18 and 19.

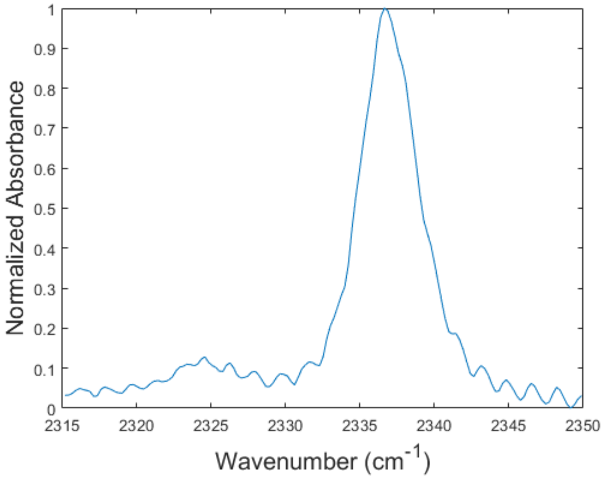

Figure 18: FTIR for the 0% ionic liquid sample by Dr. Kelsheimer. The maximum of the peak is 2337 cm^{-1}, and the HWHM is 2.5 cm^{-1} ($\frac{(2339-2334)}{2}\, cm^{-1}$).

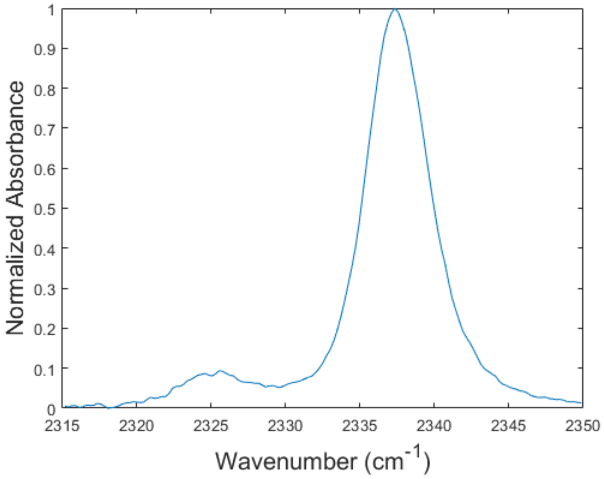

Figure 19: FTIR for the 10% ionic liquid sample by Dr. Kelsheimer. The center frequency of the peak is 2337 cm^{-1}, and the HWHM is 2.5 cm^{-1} ($\frac{(2340-2335)}{2}\, cm^{-1}$).

A series of testing was done on the data from Dr. Kelsheimer, and the result is shown in table 3. The HWHM was found in the code, but it is not clear whether she used this HWHM for all her samples or only a few of them. From the 2D spectrum, the antisymmetrical stretch center frequency for 0% sample is 2337 cm^{-1} and 2338 cm^{-1} for the 10% sample.

Table 3: Correlation Time with different center frequency and HWHM

Center Frequency	HWHM (cm^{-1})	0% IL τ_c (ps)	10% IL τ_c (ps)
Kelsheimer's (unknown)	2.3	117.8 (6.8)	225.5 (18.3)
2337 cm^{-1}	2.3	112.1(5.0)	440.1(260.6)
2337 cm^{-1}	2.5	117.2 (4.2)	424.7 (NaN)
2338 cm^{-1}	2.3	125.3 (6.0)	294.0 (28.5)
2338 cm^{-1}	2.5	125.3 (6.0)	294.0 (28.5)
2338.3 cm^{-1}	2.3	–	294.0 (28.5)
2338.4 cm^{-1}	2.3	–	236.3 (10.4)
2338.5 cm^{-1}	2.3	–	236.3 (10.4)
2338.5 cm^{-1}	2.5	–	294.0 (28.5)
2338.7 cm^{-1}	2.3	–	236.3 (10.4)
2338.8 cm^{-1}	2.3	–	167.8 (9.0)
2339 cm^{-1}	2.3	126.8 (26.4)	167.8 (9.0)
2339 cm^{-1}	2.5	126.8 (26.4)	167.8 (9.0)

Based on the result of the calculation, to replicate the calculation by Dr. Kelsheimer, the best parameter for 0% sample is 2337 cm^{-1} with HWHM being 2.5 cm^{-1}, and the best parameter for 10% sample is between 2338.7 and 2338.8 cm^{-1} with HWHM being 2.3 cm^{-1}. For 0%, the replication lies in the statistical range as Dr. Kelsheimer's, and the 10% sample should be within the range between 2338.7 cm^{-1} and 2338.8 cm^{-1}. 2339 cm^{-1} and 2335 cm^{-1} are off the center based on the result of the 2D spectrum.

Below are the original plot from the Result and Discussion section of the document with no changes:

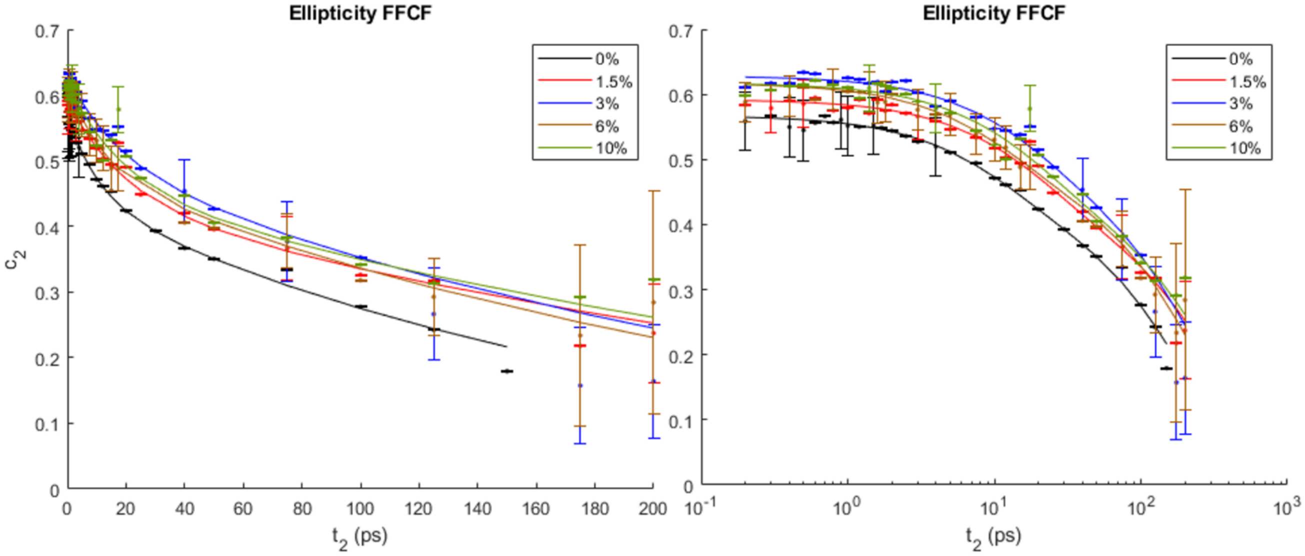

Figure 20: Biexponential fitted FFCF achieved using ellipticity in all samples. The left is the regular time-based axis, and the right is the log-based time axis. During the fitting, some of the error bars were turned off since the error was too high. The error bar in this figure is not a good indication of the realistic size of the uncertainty.

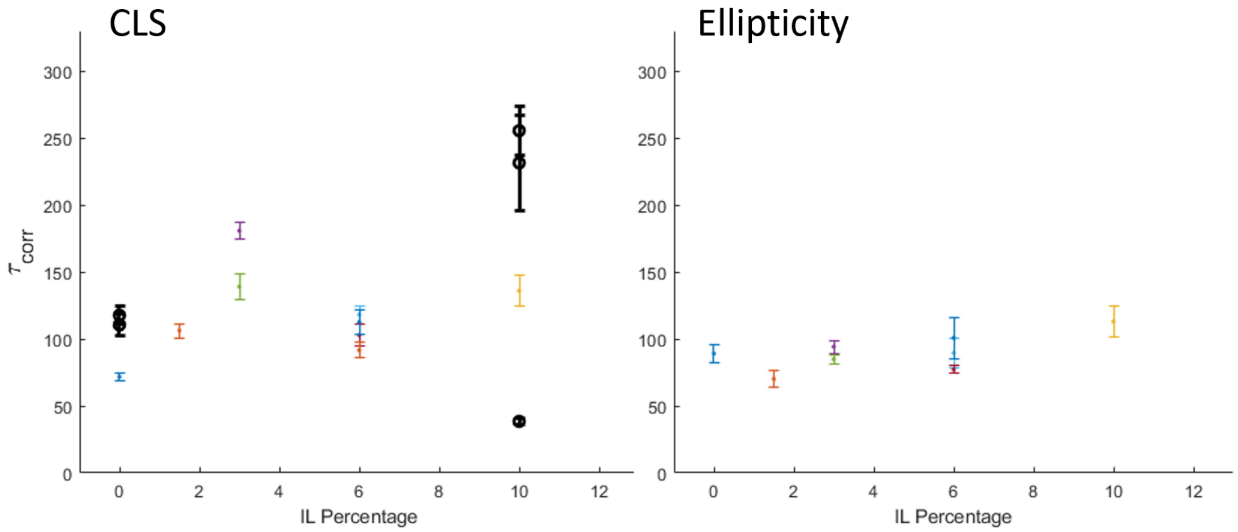

Figure 21: Correlation time for all samples analyzed using the CLS (left) and Ellipticity (on the right). Black bold timescales are the value reported previously[2].

The correlation time for all samples analyzed using CLS and Ellipticity is re-plotted here for the convenience of the following discussion, and the result from ellipticity is used for the discussion. There is a discrepancy between the FFCF extracted using ellipticity and the correlation plotted as a function of IL percentage. The plotting function is written as an individual function in Matlab, and the path of loading files is not the same as the saving path in the script for generating the plot. This means the plot of the correlation time as a function of ionic liquid concentration is not the same as the integration shown on the plot as a function of the IL concentration. After changing the path of the plotting function, the correlation function for ellipticity is regenerated in Figure 22, and the correlation time as a function of IL concentration is plotted in Figure 23.

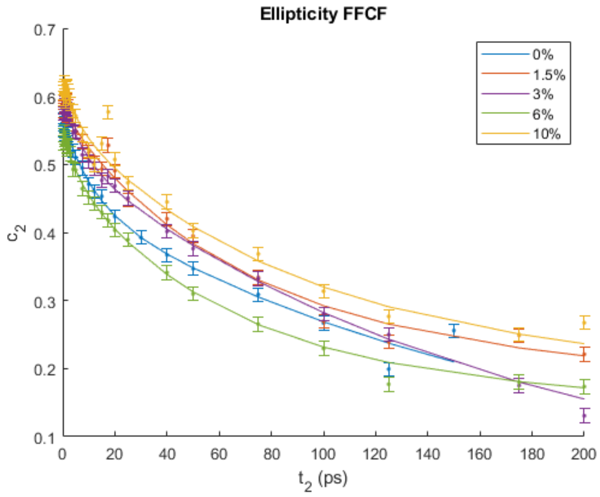

Figure 22: The FFCF extracted using ellipticity for different concentrations.

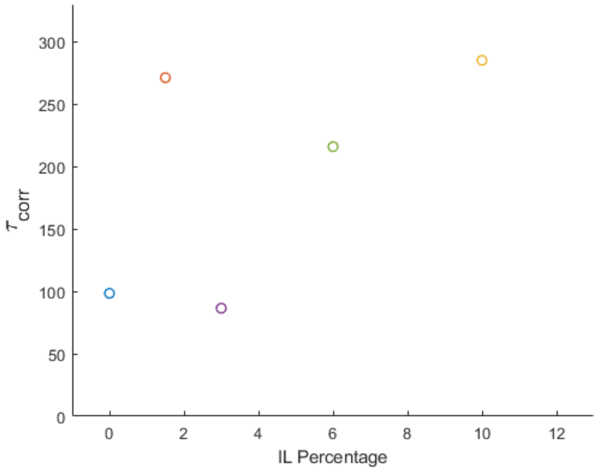

Figure 23: The correlation time integrated by each FFCF from Figure 22 is plotted as a function of ionic liquid percentage. The value is more logical compared to the previous set of figures.

The 10% sample now has the highest value in all time points, and it is logical for that data set to have the highest correlation time, which means the largest area under the curve. The result shown in Figure 23 agrees with such observation. Meanwhile, the 3% sample has the fastest decay, therefore it is logical for the area under the curve to be the smallest compared to 6%, even when 6% decays faster in early t_2. The 6% almost reached a plateau at 200 ps, but the 3% data was still decaying significantly at that time point. The result in Figure 23 shows agreement with the previous observation as well. It is logical to conclude that the correlation time as a function of ionic liquid percentage is the value under the FFCF plot for each concentration.

Based on the Figure 23, the fitted correlation functions are dominated by the longer time. More replication of the longer t_2 time will be collected with a higher signal-to-noise ratio. Another method for sample preparation will be performed. As suggested by Dr. Laaser, the concentration and homogeneous mixture will be controlled by recording the mass transfer after each step and dissolving each material in a cosolvent.

5.0 Conclusion

Besides incorporating the preferential solvation model into the system, building a model that could simulate the spectrum is another helpful to have a better understanding of the physical composition of the system. *Brinzer et al.* have shown simulated the quadrupolar local environment of CO_2 in the ionic liquid and the temperature dependence of the FFCF[21,22]. Originally, the non-polar CO_2 interacts with the side chain of the ionic liquid was thought to be the reason why CO_2 can dissolve in the ionic liquid, but the results is completely different. Therefore, in the future, building a molecular model using the preferential solvation and validating the model using the 2D-IR spectrum are crucial steps to analyze the data.

In conclusion, the dynamics of the CO_2 change as the concentration of the ionic liquid in the composite system increases. Additional measurements of different concentrations need to be performed to reach a more reliable conclusion. Simulations of the spectra using the lineshape function and response function on each set of data also need to be conducted, and the parameters in CLS and ellipticity fitting needs to be adjusted accordingly. A modification of the core-shell-matrix model using the preferential solvation is proposed, and the new correlation time would be calculated as compared to the experimental data.

6.0 Future direction

The immediate next step of the experiment is discussed at the end of Appendix B which includes enhancement in both sample preparation and 2D-IR spectrum acquisition. The next stage of this research is replacing the core-shell-matrix model with the preferential solvation model to build a simpler physical model that provides a better understanding of the CO_2 solvation dynamics in IL-polymer composite material to guide the future discovery of the CO_2 absorption material.

Bibliography

[1] Hamm, P.; Zanni, M. T. *Concepts and Methods of 2D Infrared Spectroscopy*; Cambridge University Press: New York, NY, 2011.

[2] Kelsheimer, C. J.; Garrett-Roe, S. Intramolecular Vibrational Energy Relaxation of CO 2 in Cross-Linked Poly(ethylene glycol) Diacrylate-Based Ion Gels. *J. Phys. Chem. B* **2021**, *125*, 1402–1415.

[3] Tomé, L. C.; Marrucho, I. M. Ionic liquid-based materials: a platform to design engineered CO 2 separation membranes. *Chem. Soc. Rev.* **2016**, *45*, 2785–2824.

[4] Rao, A. B. Details of A Technical , Economic and Environmental Assessment of Amine-based CO 2 Capture Technology for Power Plant Greenhouse Gas Control. Appendix to Annual Technical Progress Report. Reporting period October 2000 - October 2001. **2002**, 40.

[5] Sumida, K.; Rogow, D. L.; Mason, J. A.; McDonald, T. M.; Bloch, E. D.; Herm, Z. R.; Bae, T. H.; Long, J. R. Carbon dioxide capture in metal-organic frameworks. *Chem. Rev.* **2012**, *112*, 724–781.

[6] Qazvini, O. T.; Telfer, S. G. A Robust Metal-Organic Framework for Post-combustion Carbon Dioxide Capture. *J. Mater. Chem. A* **2020**, *8*, 12028–12034.

[7] Trickett, C. A.; Helal, A.; Al-Maythalony, B. A.; Yamani, Z. H.; Cordova, K. E.; Yaghi, O. M. The chemistry of metal-organic frameworks for CO2 capture, regeneration and conversion. *Nat. Rev. Mater.* **2017**, *2*.

[8] Li, J. R.; Ma, Y.; McCarthy, M. C.; Sculley, J.; Yu, J.; Jeong, H. K.; Balbuena, P. B.; Zhou, H. C. Carbon Dioxide Capture-related Gas Adsorption and Separation in Metal-Organic Frameworks. *Coord. Chem. Rev.* **2011**, *255*, 1791–1823.

[9] An, J.; Geib, S. J.; Rosi, N. L. High and selective CO2 uptake in a cobalt adeninate metal–organic framework exhibiting pyrimidine- and amino-decorate pores. *J. Am. Chem. Soc.* **2010**, *132*, 38–39.

[10] Schulte, Z. M.; Kwon, Y. H.; Han, Y.; Liu, C.; Li, L.; Yang, Y.; Jarvi, A. G.; Saxena, S.; Veser, G.; Johnson, J. K.; Rosi, N. L. H2/CO2separations in multicomponent metal-adeninate MOFs with multiple chemically distinct pore environments. *Chem. Sci.* **2020**, *11*, 12807–12815.

[11] Welton, T. Room-Temperature Ionic Liquids. Solvents for Synthesis and Catalysis. *Chem. Rev.* **1999**, *99*, 2071–2084.

[12] Ueki, T.; Watanabe, M. Macromolecules in Ionic Liquids: Progress, Challenges, and Opportunities. *Macromol. (Washington, DC, U. S.)* **2008**, *41*, 3739–3749.

[13] Gurkan, B.; Goodrich, B. F.; Mindrup, E. M.; Ficke, L. E.; Massel, M.; Seo, S.; Senftle, T. P.; Wu, H.; Glaser, M. F.; Shah, J. K.; Maginn, E. J.; Brennecke, J. F.; Scheider, W. F. Molecular Design of High Capacity, Low Viscosity Chemically Tunable Ionic Liquids for CO2 Capture. *J. Phys. Chem. Lett.* **2010**, *1*, 3494–3499.

[14] Blanchard, L. A.; Hancu, D.; Beckman, E. J.; Brennecke, J. F. Green processing using ionic liquids and CO2. *Nature* **1999**, *399*, 28–29.

[15] Bara, J. E.; Carlisle, T. K.; Gabriel, C. J.; Finotello, A.; Gin, D. L.; Noble, R. D.; Camper, D.; Finotello, A.; Gin, D. L.; Noble, R. D. Guide to CO2 Separations in Imidazolium-based Room-Temperature Ionic Liquids. *Ind. Eng. Chem. Res.* **2009**, *48*, 2739–2751.

[16] Kofu, M.; Someya, T.; Tatsumi, S.; Ueno, K.; Ueki, T.; Watanabe, M.; Matsunaga, T.; Shibayama, M.; Sakai, V. G.; Tyagi, M.; Yamamuro, O. Microscopic insights into ion gel dynamics using neutron spectroscopy. *Soft Matter* **2012**, *8*, 7888.

[17] Hamm, P.; Lim, M.; Hochstrasser, R. M. Vibrational Relaxation and Dephasing of Small Molecules Strongly Interacting with Water. Ultrafast Phenom. XI. BERLIN, 1998; pp 514–516.

[18] Brinzer, T.; Berquist, E. J.; Ren, Z.; Dutta, S.; Johnson, C. A.; Krisher, C. S.; Lambrecht, D. S.; Garrett-Roe, S. Ultrafast Vibrational Spectroscopy (2D-IR) of CO2 in Ionic Liquids: Carbon Capture from Carbon Dioxide's Point of View. *J. Chem. Phys.* **2015**, *142*, 212425.

[19] Berquist, E. J.; Daly, C. A., Jr.; Brinzer, T.; Bullard, K. K.; Campbell, Z. M.; Corcelli, S. A.; Garrett-Roe, S.; Lambrecht, D. S. Modeling Carbon Dioxide Vibrational Frequencies in Ionic Liquids: I. Ab Initio Calculations. *J. Phys. Chem. B* **2017**, *121*, 208–220.

[20] Daly, C. A., Jr.; Berquist, E. J.; Brinzer, T.; Garrett-Roe, S.; Lambrecht, D. S.; Corcelli, S. A. Modeling Carbon Dioxide Vibrational Frequencies in Ionic Liquids: II. Spectroscopic Map. *J. Phys. Chem. B* **2016**, *120*, 12633–12642.

[21] Brinzer, T.; Daly, C. A., Jr.; Allison, C.; Garrett-Roe, S.; Corcelli, S. A. Modeling Carbon Dioxide Vibrational Frequencies in Ionic Liquids: III. Dynamics and Spectroscopy. *J. Phys. Chem. B* **2018**, *122*, 8931–8942.

[22] Daly, C. A., Jr.; Allison, C.; Corcelli, S. A. Modeling Carbon Dioxide Vibrational Frequencies in Ionic Liquids: IV. Temperature Dependence. *J. Phys. Chem. B* **2019**, *123*, 3797–3803.

[23] Bara, J. E.; Gabriel, C. J.; Hatakeyama, E. S.; Carlisle, T. K.; Lessmann, S.; Noble, R. D.; Gin, D. L. Improving CO2 selectivity in polymerized room-temperature ionic liquid gas separation membranes through incorporation of polar substituents. *J. Memb. Sci.* **2008**, *321*, 3–7.

[24] Stacy, E. W.; Gainaru, C. P.; Gobet, M.; Wojnarowska, Z.; Bocharova, V.; Greenbaum, S. G.; Sokolov, A. P. Fundamental Limitations of Ionic Conductivity in Polymerized Ionic Liquids. *Macromolecules* **2018**, *51*, 8637–8645.

[25] Bocharova, V.; Wojnarowska, Z.; Cao, P. F.; Fu, Y.; Kumar, R.; Li, B.; Novikov, V. N.; Zhao, S.; Kisliuk, A.; Saito, T.; Mays, J. W.; Sumpter, B. G.; Sokolov, A. P. Influence of Chain Rigidity and Dielectric Constant on the Glass Transition Temperature in Polymerized Ionic Liquids. *J. Phys. Chem. B* **2017**, *121*, 11511–11519.

[26] Arora, S.; Rozon, J.; Laaser, J. E. Dynamics of Ion Locking in Doubly-Polymerized Ionic Liquids. *Macromolecules* **2021**, *54*, 6466–6476.

[27] Arora, S.; Liang, J.; Fullerton-Shirey, S. K.; Laaser, J. E. Triggerable Ion Release in Polymerized Ionic Liquids Containing Thermally Labile Diels-Alder Linkages. *ACS Mater. Lett.* **2020**, 331–335.

[28] Xie, F.; Gao, X.; Yu, Y.; Lu, F.; Zheng, L. Dually cross-linked single network poly(ionic liquid)/ionic liquid ionogels for a flexible strain-humidity bimodal sensor. *Soft Matter* **2021**, *17*, 10918–10925.

[29] Li, Y.; Wang, X.; Dong, S.; Chen, X.; Cui, G. Recent Advances in Non-Aqueous Electrolyte for Rechargeable Li–O2 Batteries. 2016.

[30] Osada, I.; de Vries, H.; Scrosati, B.; Passerini, S. Ionic-Liquid-Based Polymer Electrolytes for Battery Applications. *Angew. Chemie* **2016**, *128*, 510–523.

[31] Muldoon, J.; Bucur, C. B.; Boaretto, N.; Gregory, T.; Di Noto, V. Polymers: Opening doors to future batteries. 2015.

[32] Liang, J.; Xu, K.; Arora, S.; Laaser, J. E.; Fullerton-Shirey, S. K. Ion-Locking in Solid Polymer Electrolytes for Reconfigurable Gateless Lateral Graphene p-n Junctions. *Materials (Basel).* **2020**, *13*.

[33] Hasib-ur Rahman, M.; Siaj, M.; Larachi, F. Ionic liquids for CO2 capture—Development and progress. *Chem. Eng. Process. Process Intensif.* **2010**, *49*, 313–322.

[34] Karunaweera, C.; Li, P.; Gin, D. L.; Noble, R. D. Stable, Long-Term, High-Temperature, and High-Pressure Operation of Poly(ionic liquid)–Ionic Liquid Membranes Made with Ionic-Liquid-Based Multifunctional Cross-Linkers for CO 2 /CH 4 Separation. *Ind. Eng. Chem. Res.* **2022**,

[35] Kelsheimer, C. J. Ultrafast Vibrational Spectroscopy of Carbon Dioxide in Polymers and Ionic Liquid-Polymer Composite Materials. Ph.D. thesis, 2021.

[36] Robert Socolow,; Michael Desmond,; Roger Aines,; Jason Blackstock,; Olav Bolland,; Tina Kaarsberg,; Nathan Lewis,; Marco Mazzotti,; Allen Pfeffer,; Karma Sawyer,; Jeffrey Siirola,; Berend Smit,; Jennifer Wilcox, *Direct Air Capture of CO 2 with Chemicals Direct Air Capture of CO 2 with Chemicals A Technology Assessment for the APS Panel on Public Affairs*; 2011.

[37] Mathonat, C.; Majer, V.; Mather, A. E.; Grolier, J.-P. E. Use of Flow Calorimetry for Determining Enthalpies of Absorption and the Solubility of CO 2 in Aqueous Monoethanolamine Solutions. *Ind. Eng. Chem. Res.* **1998**, *37*, 4136–4141.

[38] Mazzotti, M. *Introduction to Chemical Engineering: Thermodynamics of Separation Processes*; ETH Zurich, Institute of Process Engineering: Zurich, Switzerland, 2020.

[39] Freeman, B. D. Basis of Permeability/Selectivity Tradeoff Relations in Polymeric Gas Separation Membranes. *Macromolecules* **1999**, *32*, 375–380.

[40] Robeson, L. M. The Upper Bound Revisited. *J. Memb. Sci.* **2008**, *320*, 390–400.

[41] Robeson, L. M. Correlation of separation factor versus permeability for polymeric membranes. *J. Memb. Sci.* **1991**, 165–185.

[42] Kwak, K.; Park, S.; Finkelstein, I. J.; Fayer, M. D. Frequency-Frequency Correlation Functions and Apodization in Two-Dimensional Infrared Vibrational Echo Spectroscopy: a New Approach. *J. Chem. Phys.* **2007**, *127*, 124503.

[43] Roberts, S. T.; Loparo, J. J.; Tokmakoff, A. Characterization of Spectral Diffusion from Two-Dimensional Line Shapes. *J. Chem. Phys.* **2006**, *125*, 84502.

[44] Hamm, P.; Kaindl, R. A.; Stenger, J. Noise Suppression in Femtosecond Mid-Infrared Light Sources. *Opt. Lett.* **2000**, *25*, 1798–1800.

[45] Helbing, J.; Hamm, P. Compact Implementation of Fourier Transform Two-Dimensional IR Spectroscopy without Phase Ambiguity. *J. Opt. Soc. Am. B* **2011**, *28*, 171.

[46] Dunbar, J. A.; Arthur, E. J.; White, A. M.; Kubarych, K. J. Ultrafast 2D-IR and Simulation Investigations of Preferential Solvation and Cosolvent Exchange Dynamics. *J. Phys. Chem. B* **2015**, *119*, 6271–6279.